UNIVERSIDADE DE LISBOA

FACULDADE DE CIÊNCIAS

DEPARTAMENTO DE FÍSICA

Ciências
ULisboa

Time of Flight Simulation and Reconstruction in Hybrid MR-PET Systems

Sara Margarida Parra Leal da Costa

Mestrado Integrado em Engenharia Biomédica e Biofísica
Perfil em Engenharia Clínica e Instrumentação Médica

Dissertação orientada por:
Prof. Doutor Nuno Matela
Doutora Liliana Caldeira

2018

Acknowledgements

I would like to start by thanking Professor Jon Shah for giving me the opportunity to work at the Institute of Neurosciences and Medicine of the Forschungszentrum Jülich in INM-4. I am thankful to be part of such an important research group and to experience a real research environment.

I would like to express my appreciation towards my supervisor, Doctor Liliana Caldeira, who guided me during my work, corrected my thesis and explained me how to work with the software tools developed at the Forschungszentrum Jülich. Also, I would like to thank Hancong Xu for helping me when my supervisor was not around. Without him this thesis would never have been successful.

I also wish to thank to my intern supervisor, Nuno Matela, for providing the contact with the PET group at the Forschungszentrum Juelich. Also, as my supervisor, his regular and prompt feedback, support and optimism were crucial in this work.

Furthermore, I would like to thank all the amazing people I met during my internship abroad, in and outside of the office. Thank you for all the amazing experiences we lived together. In particular to my colleagues of INM-4 at Forschungszentrum Juelich thank you for all the friendly talks during the lunch and for all the fun activities outside of work.

This work was only possible with the support of my family. Without their help, I would not have been able to, not only finish but even to start a new journey abroad. A special thanks to my boyfriend, André Krippahl, for all the love and support, for the trips that we made when he visited me and for his incentive during this year. I also need to thank my friends from EBB Cristiana Tiago, Inês Bagulho, Joana Guido, Rita Tomás and Sara Guerreiro, thanks for the skype calls and for the trips around Europe. I would also like to thank to my oldest friends Carolina Figueiredo, Fábio Caldeira, Guilherme Pinto, João Paulo Silva, Joana Baleiras, Margarida Ferrito, Marta Sarrico, Pedro Ascensão and Rita Fonseca for their friendship and support throughout all these years. Finally I would like to thank my friend Filipa Silva for sharing the apartment with me (for the second time in her life) and the amazing adventures that we shared during this year, inside and outside of work.

Abstract

In traditional PET, coincidence electronics are used to determine the line of response along which an annihilation has occurred. With time-of-flight(TOF), the approximate position of the annihilation along the line of annihilation is calculated by measuring the difference between the arrival time of the photons in the detectors. In the literature, TOF images show (in general) a lower level of noise and better resolution compared to non-TOF images. The lower noise and amplified sensitivity of TOF reconstruction could favour a better use of the full resolution potential of PET scanners.

The first part of this thesis focuses on the possibility of using faster simulating methods, more specifically, the possibility of replacing the time consuming GATE simulations by a script (from Paola Solevi from Otto-von-Guericke-Universität Magdeburg) was studied. The results show that the values obtained in the simulations with the Hoffman Brain Phantom are very similar between the two methods, showing the viability of this script with this phantom. Then, the same procedure was performed using a Voxelized Brain Phantom. This time the results were different from the ones obtained before because the values obtained with the two methods are very different. Therefore, it is important to know if there is some kind of problem with the phantom used that origins those results or if the problem comes from the script.

The second part of this thesis focuses on the development of reconstruction procedures for simulations done with the GE Signa PET-MR scanner. The methods includes the simulation of three phantoms (offcenter cylinder and Hoffman Brain Phantom to reconstruct and a large cylinder for the normalisation), a coordinates algorithm developed in MATLAB that can calculate the correct coordinates, for the sinograms, from the GATE coordinate output and a method that, from an uncorrected sinogram, obtains an arc corrected sinogram that can be used in reconstructions. The results show that the reconstructions were successful, without any artifacts. The reconstructions done without each one of the corrections, show artifacts in both phantoms. These results show the importance of doing corrections before reconstructing the data.

Key-words: PET-MR, BrainPET, GE Signa, TOF, GATE

Resumo

A Tomagrafia de Emissão de Positrões (PET) é uma técnica de imagem médica amplamente utilizada devido à sua capacidade de fornecer informações bioquímicas e metabólicas e é usada principalmente para a caracterização não invasiva de tumores e metástases, bem como para monitorar o efeito da terapia em casos de cancro. Esta modalidade permite então a detecção de anormalidades precoces na função ou estrutura dos órgãos, possibilitando o tratamento de certas doenças em estágios iniciais e, consequentemente, aumenta a probabilidade de recuperação do paciente. No entanto, as imagens PET não contêm informações anatómicas detalhadas e, portanto, beneficiam da fusão com informações de imagens morfológicas de outras modalidades de imagem, como a ressonância magnética (MR).

Após a injecção de um radiotraçador marcado com um radionuclídeo emissor de positrões, o sujeito é colocado dentro do scanner que possui um grande número de detectores (organizados em anéis) capazes de registar raios gama incidentes. O radionuclídeo no radiotraçador decai e os positrões resultantes, quando em contacto com electrões livres que existem na matéria, aniquilam. Cada aniquilação produz dois fotões de 511 keV que viajam em direcções opostas sendo posteriormente detados pelos anéis de detetores em volta do sujeito. A linha que liga os dois detectores, que foram atingidos pelos fotões resultantes da aniquilação, é usada para obter a imagem tomográfica e é denominada *line of response*. Sempre que uma aniquilação produza uma saída dois fotões que são registados dentro de uma janela de tempo específica, o evento é considerado uma coincidência. Estes eventos são denominados "prompts" e podem ser divididos em coincidências verdadeiras, dispersas, aleatórias e múltiplas.

Como já foi referido, a obtenção de imagens no PET é baseado nas informações obtidas a partir da *line of response* que liga os detetores onde os fotões foram detetados. No entanto, esta linha indica apenas que a aniquilação acorreu algures nessa linha mas não indica o ponto exato onde os fotões foram emitidos. O *time of flight* vai um passo à frente e tenta determinar aproximadamente a posição de aniquilação ao longo da *line of response* usando a diferença entre os tempos de chegada dos fotões aos detectores. No entanto, para este cálculo poder ser feito, é necessário que o scanner possua um valor baixo de *time*

resolution e, para isso acontecer, tem de possuir os mais recentes cintiladores bem como um maior poder de computação.

O objetivo geral desta tese é o estudo do *time of flight* em simulações e na reconstrução de imagens de dois scanners: BrainPET e GE Signa PET-MR. Uma parte deste trabalho concentra-se na comparação de dois métodos de obtenção de dados a partir de simulações realizadas com os parâmetros do BrainPET, a fim de verificar se um script pode substituir eficientemente o método mais demorado que é realizar simulações no software GATE. A outra parte desta tese concentra-se no desenvolvimento de um método para reconstruir imagens de simulações feitas com as características do scanner GE Signa PET-MR.

A tese está organizada em 6 capítulos descritos abaixo. O primeiro capítulo introduz o contexto, o objetivo e a organização geral da tese. O capítulo 2 é subdividido em 5 seções (Princípios do PET, *Time of Flight*, Aquisição de Dados, Correção de Dados e Reconstrução de Imagens). Começa com a explicação dos principios fisicos do PET e do *time of flight*. Em seguida, são explicados todos os processos pelos quais os dados devem passar para no final obter imagens PET. O capítulo 3 começa com uma breve explicação acerca das simulações de Monte Carlo e as suas aplicações na Medicina Nuclear. Depois, há uma descrição mais detalhada do software GATE que foi usado neste estudo bem como do software ROOT. O capítulo é subdividido em 6 seções (Gerador de Números Aleatórios, Aplicações em Medicina Nuclear, GEANT4, GATE, TOF GATE e ROOT). A introdução da tese termina neste capítulo.

O capítulo 4 contém os materiais, métodos, resultados e discussão do trabalho realizado com as simulações GATE do scanner BrainPET, comparando dois métodos de obtenção dos dados necessários para a reconstrução. Esta parte da tese foca-se na possibilidade de usar métodos de simulação mais rápidos que os atuais. Neste caso, é estudada a possibilidade de substituir as simulações mais demoradas feitas com o GATE por um script (que leva segundos para ser executado). Mais especificamente, é a possibilidade de obter os dados das simulações feitas com *time resolution* apenas fazendo uma simulação no GATE sem *time resolution* e depois executar o script. Primeiramente, foi necessário descobrir, através de simulações, qual a *multiples policy* mais adequada ao script. Depois de fazer as alterações necessárias para que os dois métodos tivessem os mesmos parâmetros de simulação, as simulações foram feitas com diferentes valores para a *time resolution* e a partir dos valores obtidos, alguns parâmetros foram avaliados. Estes parâmetros incluem o número de coincidências aleatórias e a sua fração em relação ao número total de coincidências e o número de coincidências dispersas e sua fração no número total de coincidências. Os resultados mostram que os valores obtidos nas simulações com o Hoffman Brain Phantom são muito semelhantes entre os dois métodos mostrando a viabilidade deste script com este fantoma. Mais tarde, o mesmo procedimento foi realizado usando um Voxelized Brain Phantom mas os resultados não foram os esperados. De facto, os valores obtidos com os dois métodos diferem bastante. Estes resultados vão contra os obtidos com o fantoma anterior e questionam a viabilidade do script. Os resultados fora do normal, como por exemplo o número de coincidências aleatórias, vêm das simulações do GATE e não do script. Os valores do script têm no geral o comportamento esperado. Portanto, é importante saber

se existe algum tipo de problema com o fantoma usado que origina esses resultados ou se o problema vem do script. É importante notar que o script não possui muitas indicações em relação aos parâmetros usados e que por isso poderá haver algum parâmetro mal definido de que não se tenha conhecimento para além daqueles estudados nesta tese (diferença mínima de sectores e *multiples policy*).

No capítulo 5 estão os materiais, métodos, resultados e respectiva discussão das simulações e dos processos de reconstrução feitos para obter imagens de dois fantomas diferentes (cilindro *offcenter* e Hoffman Brain Phantom) a partir de simulações do GE Signa PET MR feitas no software GATE. Esta parte da tese foca-se no desenvolvimento de procedimentos de reconstrução para simulações feitas com o scanner GE Signa PET-MR. Primeiro, após a aquisição de dados através de simulações, o *output* do GATE tem de ser adaptado ao *script* de MATLAB. Para isso, foi feito um algoritmo de transformação de coordenadas que tem como *output* o formato de coordenadas correto para obter os sinogramas. Depois, são obtidos os sinogramas que não possuem qualquer correção. Estes sinogramas são usados noutro script de MATLAB que faz a *arc correction* tendo como *output* sinogramas *arc corrected* que serão usados mais tarde na reconstrução. Outra correção realizada, foi a normalização. Foi feita uma simulação de um cilindro do tamanho do *field of view* cujos resultados passaram pelas etapas anteriormente referidas. Os sinogramas *arc corrected* foram então usados na reconstrução como *inputs* para a normalização. Para testar todo o processo de reconstrução desenvolvido, dois fantomas foram simulados (um cilindro *offcenter*) e um Hoffman Brain Phantom. Os resultados mostram que as reconstruções foram bem sucedidas, sem nenhum artefacto. No entanto, as imagens resultantes do Hoffman Brain Phantom tiveram baixa resolução devido ao fato de que as únicas correções feitas terem sido a "arc correction" e a normalização. As reconstruções feitas sem cada uma dessas correções mostram artefactos em ambos os fantomas mostrando a importância de fazer correções antes da reconstrução dos dados. O trabalho futuro inclui tentar a reconstrução com outros tipos de fantomas, fazer outros tipos de correções (como scatter random) e fazer a reconstrução tendo em conta o *time of flight*, uma vez que se trata do scanner com essa capacidade.

Palavras-chave: PET-MR, BrainPET, GE Signa, TOF, GATE

Contents

List of Figures

List of Tables

List of Abbreviations

2D   Twodimensional

3D   Threedimensional

APD   Avalanche photodiode

CERN European Organization for Nuclear Research

CT   Computed Tomography)

FWHM Full width at half maximum

GATE GEANT4 Application for Tomographic Emission

INM-4 Institute of Neuroscience and Medicine-4

LSO   Lutetium Oxyorthosilicate

LYSO Lutetium-yttrium oxyorthosilicate

MLEM Maximum Likelihood Expectation Maximization

MR   Magnetic Resonance

MR-PET Magnetic resonance-positron emission tomography

OSEM Ordered Subsets Expectation Maximization

PET   Positron emission tomography

PMT   Photomultiplier tube

PRNG Pseudorandom number generator

RF   Radiofrequency

SF   Scatter fraction

SiPM Silicon photomulti-pliers

SPECT Single-photon emission computed tomography

STIR Software for Tomographic Image Reconstruction

TOF   Time of Flight

Chapter 1

Introduction

1.1 Context

PET is a medical imaging technique that is widely used due to its capability of providing biochemical and metabolic information and it is mainly used for the non-invasive characterisation of tumours and metastases, as well as for monitoring effect of cancer therapy. However, PET images do not contain any detailed anatomical information and therefore benefits from the fusion with morphological image information from other image modalities like MR (magnetic resonance) or CT (Computed Tomography).

After injection of a tracer compound labelled with a positron emitting radionuclide, the subject of the PET study is placed within the field of view of a number of detectors capable of registering incident gamma rays. The radionuclide in the radiotracer decays and the resulting positrons subsequently annihilate on contact with electrons. Each annihilation produces two 511 keV photons travelling in opposite directions that are detected by the detectors in a ring around the subject.

The Siemens 3T MR-BrainPET and the GE Signa PET-MR are hybrid scanners for simultaneous acquisition of MRI and PET and the last one also possesses time-of-flight capability, achieving a time resolution of 400 ps. In traditional PET coincidence electronics are used to determine the line of response along which an annihilation has occurred. With time-of-flight(TOF), the approximate position of the annihilation along the line of annihilation is calculated by measuring the difference between the arrival time of the photons in the detectors. In the literature, TOF images show (in general) a lower level of noise and better resolution compared to non-TOF images. The lower noise and amplified sensitivity of TOF reconstruction could favour a better use of the full resolution potential of PET scanners. This can only happen if there is enough computational power.

Nowadays, Monte Carlo simulations are an essential tool in emission tomography (SPECT and PET). For many years, the Monte Carlo codes dedicated to PET and SPECT had several limitations in terms of validation, accuracy and support therefore these codes were not enough to do realistic simulations of emission tomography detector geometries. That is how GATE appeared as a object-oriented software in C++ that was initially developed to overcome limitations of existing codes. GATE can model time dependent phenomena so it is a good tool to simulate time-of-flight so that improvements can be made and tested before coming to reality. However, GATE also has its drawbacks that include long simulation times. These time constraints potentiate the development of less time consuming alternatives.

1.2   Thesis Objectives and Outline

The overall aim of this thesis is the study of time of flight in the simulation and reconstruction of images. A part of this work focuses on the comparison of two methods of obtaining simulated data, in order to check if a script can efficiently substitute the time consuming method that is doing the simulations using GATE software. The other part of this thesis focus on the development of a pipeline method to reconstruct images from simulations done with the GE Signa PET-MR scanner characteristics. The thesis is organized in 6 chapters described below. The current chapter introduces the context, aim and the general organization of the thesis.

Chapter 2 is subdivided in 5 sections (Principles of PET, Time of Flight, Data Acquisition, Data Correction and Image Reconstruction). It starts with the explanation of the PET basic physics and the time of flight technique. Then it describes all the processes that data must go through in order to obtain PET images.

Chapter 3 begins with a brief explanation of Monte Carlo Simulations and its applications in Nuclear Medicine. Afterwards, there is a more detailed description of the GATE software that was mainly used in this study and the ROOT software as well. The chapter is subdidvided in 6 sections (Random Number Generator, Applications in Nuclear Medicine, GEANT4, GATE, TOF GATE and ROOT).

Chapter 4 contains the materials, methods, results and discussion of the work done with the GATE simulations of the BrainPET scanner, comparing two methods of obtaining the data needed for the reconstruction.

On chapter 5 there is the materials, methods, results and respective discussion of the simulations and the reconstruction processes done in order to obtain images from the GE Signa PET MR scanner simulations on GATE.

Finally, chapter 6 includes the conclusions of all the work presented in the thesis and the perspectives for the future as well.

Chapter 2

Positron Emission Tomography

Hybrid MR-PET (magnetic resonance-positron emission tomography) systems have recently started to be more used and have the potential to change medical imaging by providing combined anatomical and metabolic image with high resolution. Especially in cancer patients, this may be beneficial.

Positron emission tomography (PET) provides means of examining cerebral blood flow, metabolism and pharmacology in vivo under both resting and activating conditions. These molecular imaging techniques are build on radiolabeled molecules (tracers) that connect to enzyme sites or surface receptors. PET utilizes short-lived positron emitting isotopes (^{15}O, ^{13}N, ^{11}C and ^{18}F) and it comes as an alternative to SPECT since it is more sensitive and versatile and allows scatter correction to be performed. SPECT is, however, cheaper and more widely available as it does not rely on a local cyclotron for production of isotopes [1]. PET is becoming increasingly important for diagnostic and treatment monitoring with a demand for better imaging quality, accuracy and speed [2].

PET is a medical imaging technique that is widely used due to its capability of providing biochemical and metabolic information and it is mainly used for the non-invasive characterisation of tumours and metastases, as well as for monitoring effect of cancer therapy. However, PET images do not contain any detailed anatomical information and therefore benefits from the fusion with morphological image information from other image modalities like MR (magnetic resonance) or CT (Computed Tomography). In the last few decades there has been an increasing interest in multimodal imaging, especially in the field of nuclear medicine. Hybrid systems allow simultaneous acquisition (intrinsically align multi-modality image information within a single exam) of two modalities and besides integrating the strength of both modalities they also eliminate some weaknesses of the individual modality. As a result, PET-CT systems started to be more used in oncological PET examinations and have proven to have a better diagnostic tool

than separate PET or CT imaging in a number of clinical indications [2]. One example of these scanners, developed and fabricated by Siemens, can be seen on Figure 2.1 on the left. More recently, hybrid MR-PET scanners were introduced and came to replace CT in this context. Comparing with PET-CT, PET-MR provides high spatial resolution (anatomical, functional and molecular imaging) and high soft tissue contrast, and a significant reduction on radiation exposure to patients. At the same time, allows different applications from functional imaging (fMRI), spectroscopy, diffusion imaging and perfusion imaging. PET-MRI also provides shorter acquisition times, allows exact spatial and temporal images coregistration and contrary to PET-CT, PET-MRI has a simultaneous acquisition and therefore the patient does not have to be repositioned for the two acquisitions [3]. A Siemans Biograph PET-MR scanner can be seen on Figure 2.1 on the right.

Figure 2.1: Siemens Biograph PET CT Scanner (on the left) taken from [4] and Siemens Biograph mMR MR/PET Scanner taken from [5]

However, MR-PET is more costly and with a lower throughput than PET-CT. Besides having its disadvantages compared to CT, MR can be considered a functional imaging technique in addition to its anatomical capabilities. This may be of particular relevance in cancer patients planning therapy and for monitoring response to treatment. Compared to CT, the anatomical capabilities of MRI are superior due to better soft-tissue contrast.

2.1   Principles of PET

PET is a nuclear medicine imaging method, frequently used in oncology for the past few years. It is a non-invasive technique that provides quantitative in vivo assessment of physiological and biological phenomena using a radiotracer in the body. This medical exam provides information that would only be available with surgeries or other invasive exams. Therefore, this modality allows the detection of early abnormalities in the function or structure of the organs, enabling treatment in initial stages and it consequently increases the probability of patient recovery.

2.1.1 Radiotracers

Before the data acquisition, PET scans require that a radiopharmaceutical or radiotracer is administered to the patient, in a small amount, by inhalation, deglutition or mainly intravenously. The injected patient dose has an optimum value that changes from patient to patient: if this dose is too low there will not be sufficient data for statistics calculations and the image will not represent the true tracer distribution. On the other hand, if the dose is too high it can be dangerous for the patient [6].

Radionuclides are chemically incorporated into a biological molecule that subsequently will be involved in a metabolic process. This is distributed throughout the body according to the chemical structure of substrate-radionuclide complex that has different tissues. Therefore, the choice of radiopharmaceutical will depend on the desired study. PET radiopharmaceuticals are based on four major, cyclotron produced, radioisotopes (^{15}O, ^{13}N, ^{11}C and ^{18}F) [7]. The short half-life of ^{15}O, ^{13}N and ^{11}C make clinical applications quite difficult or impossible in a large number of institutions: the need for an on-site cyclotron is needed which makes it difficult for some institutions to have it. In addition, the short half-life requires a very rapid conversion from the isotope to the appropriate radiopharmaceutical (which is often difficult to achieve) and requires a scheduling accuracy (availability and readiness of both patient and imaging instrument). All of these disadvantages make achieving a successful study difficult.

The most commonly used isotope in PET scans is ^{18}F. It is a fluorine isotope with a half-life of approximately 110 minutes. This tracer is very useful thanks to its long half-life and because it decays by emitting positrons having the lowest positron energy that contributes to the acquirement of an high resolution image. Most articles have considered the utility of fluorodeoxyglucose (^{18}F combined with deoxy-glucose) which is the most used radiotracer in clinical practice. The molecular structure can be seen on Figure 2.2. Actually, a number of new compounds with promising prospective for PET imaging are also available to gain information about specific cellular and molecular tumour pathways [6].
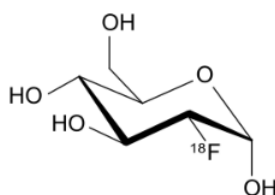
Figure 2.2: Fludeoxyglucose (also called fludeoxyglucose and fluorine-10 labeled) molecule is the most widely used PET tracer [8]

2.1.2 Interaction with Matter

In PET there are two types of radiation that interact with matter during the imaging process: charged particles (such as α particles and β particles) and electromagnetic radiation (such as γ rays and X rays). These radiations transfer their energy to the matter as they pass through it and even though they have the same principles mechanisms for energy transfer (ionization and excitation of atoms and molecules), their interaction with matter is different [9].

2.1.2.1 Interaction of Positrons with Matter

The positron ($\beta+$) is a charged particle with the same mass as the electron but with a positive charge. It is a light charged particle so it moves in a zigzag path in the matter. This energetic charged particle, loses its energy while passing through matter by interacting with the orbital electrons of the atoms in the matter. Light charged particles deposit energy through two mechanisms: collisional losses and radiation losses. Collisional losses include the energy losses by ionisation and excitation and radiation losses include the encounters that result in Bremsstrahlung production [9].

The collisions that occur between the charged particle and the atoms or molecules involve electrical forces of attraction or repulsion and not mechanical contact. For example, a charged particle passing near an atom exerts electrical forces on the orbital electrons of that atom. If it is close enough, the strength of the forces may be sufficient to cause an orbital electron to be separated from the atom, ionising it (Figure 2.3) [10]. In this interaction, the incident charged particle transfers some energy to the electron. Part of this energy is used to overcome the binding energy of the electron to the atom and the rest is given to secondary ejected electron to be used as kinetic energy.

If a charged particle passes further way from the atom, it causes the excitation of the atom without ionisation. The energy transferred to an atom in an excitation interaction is dissipated therefore this interaction usually involves a smaller energy transfer when compared with the interaction described before [10].

Finally, Bremsstrahlung (German for "braking radiation") is the electromagnetic radiation produced when the positron is deflected and decelerates due to the strong electric field. The positron penetrates the orbital electron cloud of the atom and interacts with its nucleus (Figure 2.3). The moving particle loses kinetic energy, which is converted into radiation, satisfying the law of conservation of energy. The energy of Bremsstrahlung photons can range anywhere from nearly zero (events in which the particle is only slightly deflected) up to a maximum equal to the full energy of the incident particle (events in which the particle is virtually stopped in the collision) [10].

In PET, since the photons trajectories are very irregular, when the positron is emitted, it will travel a short distance (1 mm) within the body. Then, it will finally interact with an electron leading to the conversion
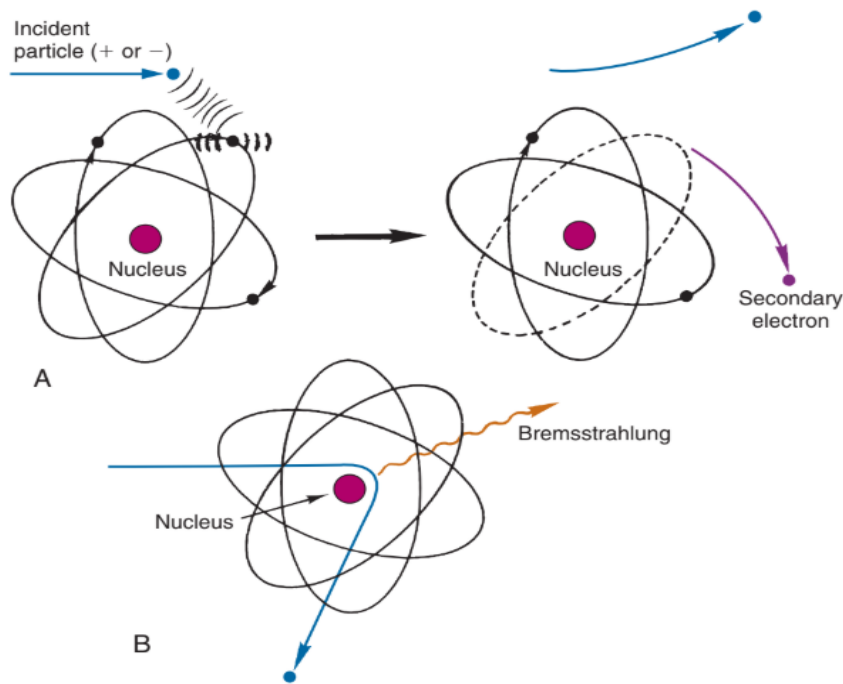
Figure 2.3: Interaction of charged particles with matter: (A) Ionisation; (B) Bremsstrahlung Production [10]

of both masses into energy. This is called annihilation and it results in the emission of two 511 keV anni-hilation photons in opposite ways. If the positron is at rest, due to conservation of momentum and energy, the photons will be emitted at an angle of 180° and then detected by opposing detectors. However, since both particles are not exactly stationary upon their interaction, some small deviation from the perfect 180° difference occurs. The angular deviation from 180° ($\pm$0.5°) is known as non-collinearity and it is independent of the radionuclide. This non-collinearity of the annihilation photons and the positron range are two physical factors that limit the spatial resolution of PET [9].

2.1.2.2   Interaction of Photons with Matter

The interaction of photons with surrounding matter is significant in PET. Photons are high-frequency radiations that interact with matter manly through 3 interactions: photoelectric effect, Compton scattering and pair production. They can be seen on Figure 2.4 and will be explained in the next sections.

Photoelectric Effect

In the photoelectric effect, a gamma radiation, while passing through an absorber, undergoes an interac-tion with an electron which is bound in an atom. In this interaction, the gamma ray transfers its entire energy primarily to an inner shell electron of an absorber atom and ejects the electron (Figure 2.4) [9]. The kinetic energy of the ejected electron (E_e) is equal to the incident gamma ray energy (E_γ) minus the binding energy of the electron in its original shell (E_b) as seen in Equation 2.1. Therefore, electrons

7
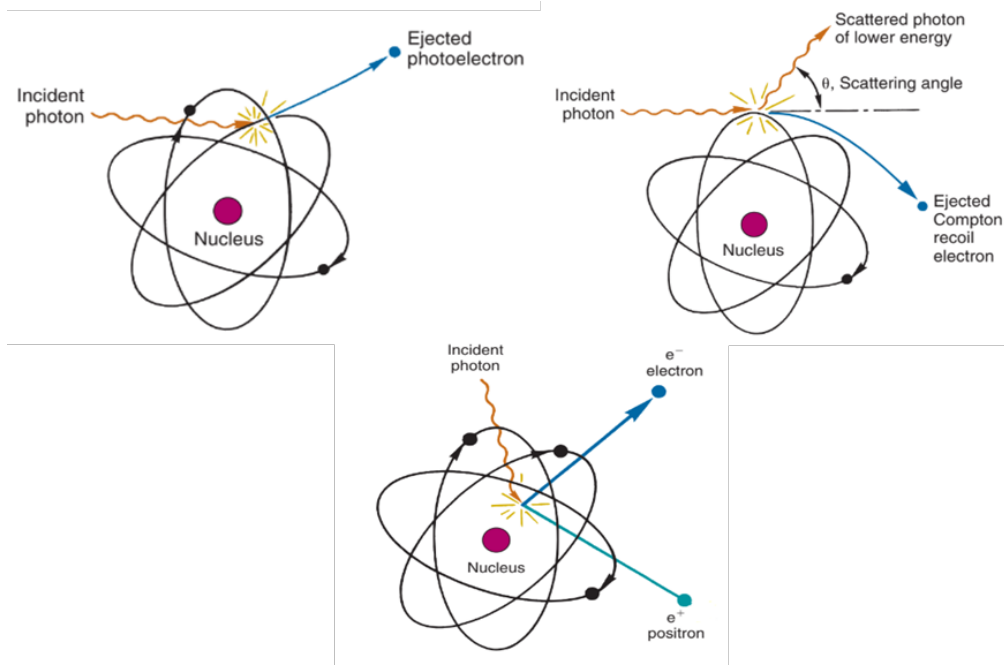
Figure 2.4: Interaction of gamma photons with matter: photoelectric effect (top-left), Compton scattering (top-left) and pair production (bottom) [10]

are only emitted by the photoelectric effect if the gamma ray reaches or exceeds a threshold energy (the binding energy of the electron). For photons with energies of more than hundreds keV, the electron carries off the majority of the incident gamma ray energy.

$$E_e = E_\gamma - E_b \tag{2.1}$$

The probability of this process decreases with increasing energy of the gamma ray but increases with increasing atomic number of the absorber (Equation 2.2).

$$P = \left(\frac{Z}{E_\gamma}\right)^3 \tag{2.2}$$

When the ejection occurs, a vacancy is formed in the atom. This vacancy in the shell is filled in by the transition of an electron from the upper shell, which leads to the emission of a characteristic x ray with an energy equal to the energy difference between the shells. It can happen that a second electron is also ejected from the outer shell leaving two vacancies. This electron is called Auger electron [10].

Compton Scattering

Compton scattering is an inelastic scattering of a gamma ray photon by a charged particle. This is usually an outer shell electron of the absorber atom and when the photon interacts with the electron, transfers part of its energy to it, ejecting the electron (Figure 2.4) [10]. The affected electron is known as recoil

electron. The energy transferred to the recoil electron can vary from zero to a large fraction of the incident photon energy because all angles of scattering, from nearly 0 ° to 180 °, are possible.

Imposing conservation of momentum and energy leads to a simple relationship between the energy of the original photon (E_γ), the energy of the scattered photon (E_{sc}), and the angle through which it is scattered (θ) that gives the energy of the scattered electron and can be seen on Equation 2.3 [11].

$$E_{sc} = \frac{E_\gamma}{1 - \frac{E_\gamma}{m_e c^2}\left(1 - \cos\theta\right)} \tag{2.3}$$

where is m_e is the mass of the electron and c is the speed of light. This is known as the rest-mass energy of the electron and is equal to 0.511 MeV. The energy transferred does not depend on the density, atomic number or any other property of the absorbing material since this interaction is a photon-electron interaction.

Pair Production

For photons with high energy (MeV or higher), pair production is the dominant mode of photon interaction with matter. If the photon is near an atomic nucleus, the energy of a photon can be converted into an electron-positron pair as shown in Equation 2.4 and ilustrated on Figure 2.4 [10].

$$\gamma \longrightarrow e^- + e^+ \tag{2.4}$$

In order for electron-positron pair production to occur, the electromagnetic energy of the photon must be above a threshold energy, which is equivalent to the rest mass of two electrons. The threshold energy (the total rest mass of produced particles) for electron-positron pair production is equal to 1.02 MeV (2 x 0.511 MeV). If the original photon's energy is greater than 1.02 MeV, any energy above 1.02 MeV is, according to the conservation law, split between the kinetic energy of motion of the two particles. The probability of pair production increases with increasing photon energy above 1.022 MeV

The photon must be near an heavy nucleus in order to satisfy conservation of momentum, as an electron-positron pair producing in free space cannot both satisfy conservation of energy and momentum [9].

2.1.3   Annihilation Detection

After injection of a tracer compound labelled with a positron emitting radionuclide the subject of a PET study is placed within the field of view of a number of detectors capable of registering incident gamma rays. The radionuclide in the radiotracer decays and the resulting positrons subsequently annihilate with electrons after travelling a short distance (1 mm) within the body. Each annihilation produces two 511

keV photons travelling in opposite directions. On Figure 2.5 it is illustrated the basic biophysics of PET technology that were just described.
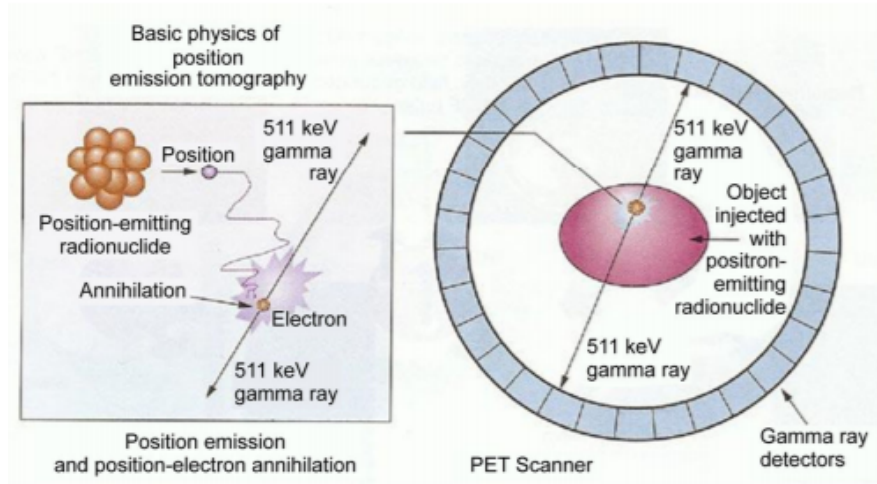
Figure 2.5: Representation of the basic biophysics of PET technology

The line connecting the two detectors that were hit by the annihilation photons is called line of response or tube-of-response, depending on the model used for reconstruction and it is used to obtain the tomographic image. With the line of response, the positional information is gained from the detected radiation without the need for a physical collimator. This is known as electronic collimation. This collimation has two major advantages over physical collimation: improved sensitivity and uniformity [12]. These coincidence events can be stored in arrays corresponding to projections through the patient and reconstructed using standard tomographic techniques. The resulting images show the tracer distribution throughout the body of the subject.

2.1.4 Types of Coincidences

The annihilation coincidence detection produces an output whenever two events are recorded within a specific coincidence time window and these are called prompt coincidences. These can be divided into true, scatter, random and multiple coincidences (shown in Figure 2.6).

As mentioned above, the total counts measured during a PET scan are called prompts. It includes every in-time coincidence and include true, scattered and random events (Equation 2.5) that are going to be explained in the next few sections.

$$P = T + S + R \qquad (2.5)$$
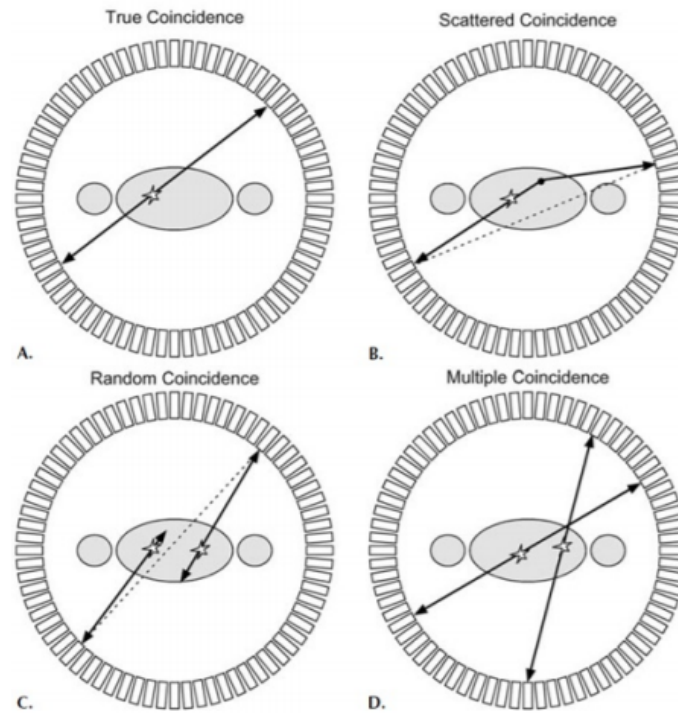
Figure 2.6: representation of different types of coincidences: (A) True Coincidence; (B) Scatter Coincidence; (C) Random Coincidence; (D) Multiple Coincidence [13]

2.1.4.1 True Coincidences

Two photons are emitted in opposite directions and will travel until they are detected by a detector pair. When the first photon of the pair is detected, there is a timing window in which the system will accept the arrival of the second photon to the other detector. This window is limited by the time resolution of the electronic components of the scanner. If the second photon is not detected on time, the event will be rejected.

If the photons come from the same annihilation then it can be said that it is a true coincidence but a complete definition says that event is considered a true event when both photons coming from the same annihilation are detected in coincidence, neither photon undergoes any form of interaction prior to detection and no other event is detected within the coincidence time window.

If it is considered a true coincidence then it is possible to draw a line of response between the two detectors that indicates that the annihilation occurred along that line. However, it must be taken into account that before annihilating with a electron, positron will travel a small distance (few millimetres). Therefore, the line of response is related to the place where the annihilation occurred and not where the positron was emitted [10].

2.1.4.2   Scatter Coincidences and Scatter Fraction

Sometimes one of the photons (or both) can interact with the surrounding tissue (or even with the detectors material) usually by Compton interactions. Due to this, the photons energy and therefore direction is changed leading to their absorbency or scattering out of the detection channel (volume between two detectors where an annihilation is recorded) so the photon ends up being assigned to a wrong line of response. Because of this, several annihilation photons are not detected [9].

Scattered coincidences add a background to the true coincidences distribution (due to radioactivity outside the field of view) which changes slowly with position, decreasing contrast and causing the isotope concentrations to be overestimated and also add statistical noise to the signal [12]. Therefore the number of coincidences measured in each channel must be corrected. This is called attenuation correction. Additionally, the scatter correction must be performed by calculating the number of scatter coincidences and subtracting them from the number of coincidences in each detection channel. Also, to limit the number of events with substantial out-of-plane components, shielding can be used in front of and behind the detector ring and it is called septa [14].

The amount of scatter existing in the image depends on numerous factors: activity distribution, object being imaged and camera geometry. The percentage of scatter coincidences in a real scanner is around 30% [9] and usually it is not below 10% or over 40%.

Assessment of PET scanner performance is mandatory to prevent image artifacts and to assure quantitative integrity of the acquired data. One of the parameters used to analyse the performance of PET scanners is the scatter fraction (SF). It is given by Equation 2.6 where SC is the number of scatter coincidences and TC is the number of true coincidences. The scanners have better image quality (therefore a better performance) when the SF has a lower value.

$$SF = \frac{SC}{SC + TC} \tag{2.6}$$

2.1.4.3   Random Coincidences and Random Fraction

Other events can take place in that coincidence time window. It can happen that two annihilation photons that come from two unrelated annihilations are detected in two different detectors inside the coincidence time window and so they are recorded as a coincidence event. This can not be considered a true coincidence but instead a random coincidence.

The rate at which random coincidences are measured between detectors A and B is given by

$$RC = 2\tau A^2 \tag{2.7}$$

where A is the activity in the scanner field of view and 2τ is the size of the timing window. This timing window is set large enough to allow true events to be accepted, but small enough to exclude as many random events as possible [14].

However, the random correction techniques result in propagation of noise through the data set so the signal to noise ratio suffers. So the best way to improve image quality without reducing the signal to noise ratio is to minimise the number of random coincidences. From Equation 2.7 it can be seen that the number of random coincidences is proportional to the coincidence time window so a small time window helps reducing the number of random coincidences. Consequently, fast scintillators with good timing resolution are the better option to reduce the number of random coincidences.

The total number of random coincidences detected also depends on the volume and attenuation characteristics of the object being imaged and on the geometry of the camera. The distribution of random coincidences is fairly uniform across the field of view, and will cause isotope concentrations to be overestimated and also add statistical noise to the data.

The random fraction calculates the percentage of randoms in the number of total coincidences (Equation 2.8). Like the number of random coincidences, this value decreases with a smaller coincidence time window and less activity.

$$RF = \frac{RC}{TC} \tag{2.8}$$

2.1.4.4 Multiple Coincidences

Multiple coincidence events happen when more than two photons are detected within a coincidence time window. Several methods can be applied but usually this events are discarded.

2.2 Time of Flight

PET is based on the principle of opposed 511 keV photons originating from the annihilation of a emitted positron with a nearby electron but there is no information about the point where those photons were emitted. In conventional PET coincidence electronics are used to determine the line of response along which an annihilation has occurred. Time-of-flight (TOF)-PET goes one step further and tries to determine approximately the position of annihilation along the line of annihilation using the measured difference in arrival times as seen in Figure 2.7.

If the difference in the arrival times of the photons is Δt, the location of the annihilation event is given by
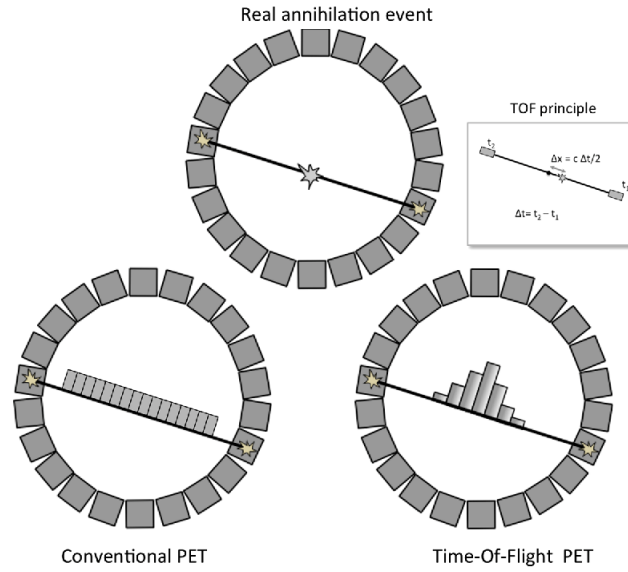
Figure 2.7: How to determine the point of annihilation along the LOR in conventional PET and in TOF PET [15]

$$\Delta d = \frac{\Delta t \times c}{2} \qquad (2.9)$$

where c is the speed of light ($3 \times 10^8 \ \mathrm{m \, s^{-1}}$). With the fastest available scintillators and careful design of the electronic components, the timing resolution can reach a few hundred picoseconds [16]. To provide useful time of flight information, the fastest and brightest scintillators need to be used.

When using the back projected reconstruction, all the voxels from the line of response have the same probability. When using time of flight information, a localisation of the event is given and the event is back projected with a probability that follows a Gaussian distribution centered on Δd from the center of the scanner and a full width at half maximum (FWHM) equal to the time resolution of the detectors.

2.2.1 PET detectors

Detection systems are a key component of any imaging system. Scintillation detectors are the most common and successful mode for detection of 511 keV photons in PET imaging. This is due to their good stopping efficiency and energy resolution. These detectors consist of an appropriate choice of crystal (scintillator) coupled to a photodetector for detection of the visible light.

In order to extract as accurately as possible information about the arrival time difference of the two annihilation photons, both components of the PET detector, namely the scintillator and the photo-detector, should have a fast, ideally instantaneous response. However, the statistical nature of radiation detection always exists, even in the case of very fast response.

2.2.1.1 Scintillators

A scintillator is a material with the ability to absorb ionizing radiation, such as X or gamma rays. It coverts a fraction of the absorbed energy into visible or ultraviolet photons that can take some nanoseconds (or even microseconds) to be performed. The brief pulse of photons corresponding to each X or gamma ray that interacts with the scintillator material, has an intensity proportional to the energy deposited in the scintillator. This pulse is sensed by the photodetector that converts it into an electrical signal [17].

In order to detect the 511 keV photons originated in the annihilation, inorganic single-crystal scintillators are used. They are chosen because of their characteristics such as generally higher density and atomic number, which leads to better detection efficiency [18] as it will be explained later.

The idea of using TOF information to localise the annihilation point along the line of response was first thought in the 1960s but only in the 1980s the first TOF PET machines were developed for clinical use. These first systems used CsF and later BaF_2 as scintillators and had a time resolution around 750 ps [19]. Since these crystals were larger, the system spatial resolution in this TOF PET systems was poor and the SNR gains were not big enough to compensate the lower detector sensitivity.

In the mid 1990s, the Lutetium Oxyorthosilicate (LSO) scintillators started to be used since they provided a combination of high light output and high stopping efficiency for 511 keV photons [20]. The immediate advantages of these crystals were the ability to have an high count-rate capability, reduced random coincidence rate and good timing resolution (450-500 ps range) [21].

Later, the discovery of cerium-doped lanthanum bromide ($LaBr_3$) opened another avenue for TOF instrumentation. While lanthanum bromide showed lower stopping power than LSO, it had shorter decay time, excellent energy resolution and twice as much light output (Table 2.1), making it more attractive for TOF-PET [22].

More recently, the first commercial time of flight PET scanner, the Gemini TF PET/CT, was introduced by Philips in 2006 using Lutetium-yttrium oxyorthosilicate (LYSO) scintillator crystals [23]. LYSO is a material with a structure very similar to LSO the difference being in the lutetium atoms in the crystal that are replaced with yttrium. LYSO properties are also very similar to those of LSO, the main difference being the lower density due to yttrium's lower weight.

As we can see, for the past few decades there has been considerable research and development of inorganic scintillators for PET imaging and the search for the ideal scintillator has been intensified for the last few years. The ideal scintillator is considered to have high light output, high stopping power and short scintillation decay time. A high light output detector produces a well-defined pulse that results in a better energy resolution. The stopping power is the mean distance that the photon travels until complete deposition of its energy and depends on the effective atomic number and density of the material. The

shorter scintillation decay time contributes to a higher efficiency at high count rates.

In order to have a better overview, the main characteristics of the major scintillators used in PET are summarized in a table for a better comparison (Table 2.1). This table is based on the intrinsic characteristics of the material and based on numerous studies over the years [9]. Each material has its advantages, however, it is possible to see that the most recent ones have better overall characteristics and that is why that have a better performance: LSO and LYSO are the most widely used scintillators in current PET detectors.

Table 2.1: Most relevant properties of the scintillators that are used in PET. It is possible to see that each material has its own advantages however but also that the more recent ones have a better overall characteristics and that is why they have a better performance [9]

Scintillator Material	Effective Atomic Number (Z)	Density (gcm^{-3})	Decay Time (ns)	Energy Resolution (% at 511 keV)
CsF	53	4.64	0.5	25.3
BaF$_2$	54	4.89	0.6	11.4
LaBr$_3$	47	5.30	25.0	5.3
LSO	66	7.40	40.0	10.1
LYSO	65	7.20	50.0	20.0

2.2.1.2 Photodetectors

The photodetectors convert the scintillation light into a fast electrical signal. The detectors usually used in PET have a finite time resolution of a few nanoseconds allowing the detection of photon events within a predefined time window. The width of this window is usually chosen to be twice the time resolution of the PET detectors [24]. The photodetectors properties affect the timing performance of the scanner so PET detectors are required to have a fast response so a good timing performance is achieved.

Photomultiplier Tubes

The photomultiplier tube (PMT) is a photo-detector type commonly used for scintillator readout in numerous applications including PET. PMTs are members of the class of vacuum tubes, and more specifically vacuum phototubes. They are extremely sensitive to light in the ultraviolet, visible, and infrared ranges of the electromagnetic spectrum. These detectors multiply the current produced by incident light (100 million times), in multiple dynode stages, enabling individual photons to be detected when the incident flux of light is low.

In TOF-PET, PMTs are still considered to be the gold standard for sub-nanosecond time resolution [25]. Their high gain combined with a low excess noise factor leads to minimal deviation from Poisson statistics as well as reduced statistical uncertainty in the generated charge signal [24].

Silicon Photomultipliers

When the first efforts were made to join the modalities of PET and Magnetic Resonance, one of the first issues was with the PET detectors since the PMTs usually used in PET scanners are not magnetic friendly. The PMTs rely on the acceleration of electrons between several dynodes and these electrons are deflected by strong magnetic fields that prevent they operability in Magnetic Resonance scanners. Therefore, they need to be replaced by another kind of detectors. Also, even though the use of photomultipliers was widely spread in PET scanners, there is another type of photodetectors that have the potential to improve PET scanners time resolution. These are called silicon photomultipliers (SiPM) [26].

Each SiPM pixel is subdivided into an array of a few thousand tiny sub-pixels that operate in Geiger mode. The Geiger mode implies that the output signal from a sub-pixel is independent of the number of the photons that hit it but also each sub-pixel is small enough so that only one photon per event will affect it [26].

These photodetectors are usually faster than the conventional PMTs and possess a longer decay time when compared with them. Their reported quantum efficiency is around 50 percent even though is difficult to quantify it since there is a lack of standardised measurement method.

Avalanche photodiodes

An avalanche photodiode (APD) is a silicon-based semiconductor containing a positive-negative (pn) junction consisting of a positively doped (p) region and a negatively doped (n) with a neutral region between them. When a scintillation photon arrives at the photodetector, it creates an electron-hole pair from the interaction in the neutral region. Afterwards, these produced electrons will ionise other atoms in a specific part of the neutral region, the avalanche region, producing more electrons. The resulting electron avalanche can produce gain factors up to several hundred [27].

They are compact and immune to magnetic fields, require low currents, are difficult to overload, and have a high quantum efficiency that can reach 90 percent. Avalanche photodiodes are now being used as an alternative to photomultiplier tubes for many low-light-level applications [27]. The disadvantages of APDs are the possibility of requiring an high operating voltage and and also produce much higher levels of noise than PMTs.

2.3 Data Acquisition

As it was mentioned previously, photons that are detected within the same time window are called prompts and they include true, random and scatter coincidences. In order to reduce the number of scatter and random events, annular septa (made of tungsten or lead) are added between the rings of the scanner. These septa can be retractable or fixed and in some scanners they are not even incorporated. Because of the septa, only direct coincidences events (true coincidences) between detectors within the

same ring or lying in closely neighbouring rings are recorded (Figure 2.8). A scanner with N rings will have N sinograms from direct planes and N - 1 sinograms from cross planes, which equals a total of 2N - 1 sinograms. The septa will drastically reduce the number of scatter and random events that reach the detectors since they are stopped by the septa. It is reported that the use of septa reduces the percentage of scatter from 30-40% to 10-15% [9]. Scans obtained with the septa in place are called twodimensional (2D) scans.
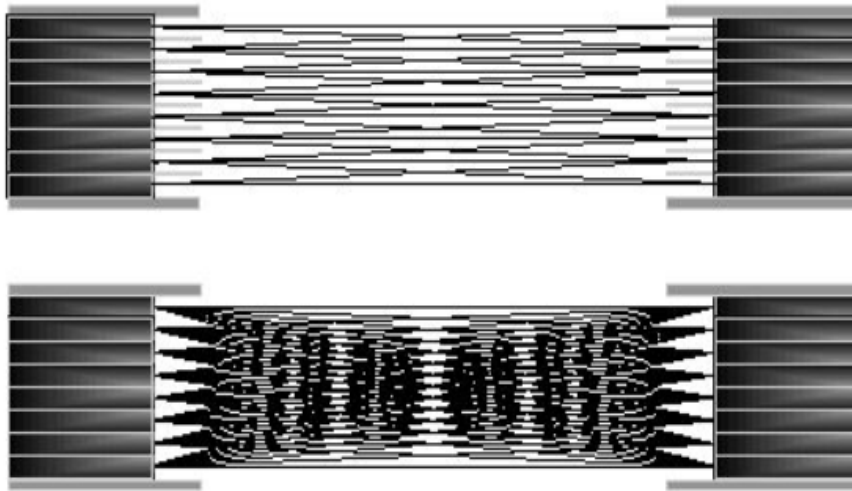
Figure 2.8: Axial cut-away view of a PET camera in 2D and 3D mode showing how the number of possible lines of response in each mode. In 2D mode only the coincidences between detectors of the same or neighbouring rings are allowed. In 3D mode coincidences between any pair of rings are allowed [28]

In a 2D acquisition data is collected for lines of response that are within the same transaxial plane (each ring can be treated separately). This approach wastes a lot of data because many photons originated from valid coincidence events are rejected by the septa, reducing the sensitivity. In threedimensional (3D) mode acquisition there is no septa so the data is obtained from all the possible lines of response, including the lines of response that connect elements in different rings (oblique lines of response) as seen in Figure 2.8. If a scanner has N rings the number of sinograms should be equal to N^2 since all ring combinations are allowed. One of the disadvantages of the 3D mode is the huge size of the data collected, hence methods of reduction of the size of data collected in 3D mode are employed [10] diminishing the number of sinograms. Also, the removal of the septa will increase sensitivity but decreases resolution if corrections for scatter and random events are not applied.

2.3.1 Sinograms

When an annihilation event occurs, the photons that are emitted form a line of response, between the detectors in which they are detected, along which the annihilation occurred. However, the specific point

of that line where the annihilation occurred is not known. The only information known is the position of the two detectors in the scanner. From that information, it is possible to know the position of the line of response [9].

The most common approach used to histogram PET data is the sinogram. The sinograms are a Random transform of the emission data in which a line along a particular radial offset and angle is mapped into a position in a matrix as shown in Figure 2.9. Essentially, each line of response is characterised by the shortest distance to the center of the scanner and its angle of orientation [29]. For example, in Figure 2.9 (left), one can see numerous lines of response that pass through a tumour near the center of the scanner (represented by an X). On Figure 2.9 (right), a sinogram is plotted for all the lines of response, that are represented on the scanner on the left side of the figure, based on the angle of orientation and distance from the scanner center. In the sinogram, the angle of orientation is plotted on the y-axis and the shortest distance to the scanner center is plotted in the x-axis. If a large number of lines of response passes through the same point, the sinogram will be half of a sine wave, as seen in Figure 2.9 (right). A more complicated object will cover many pixels therefore, its sinogram will consist on many overlapped sine waves.
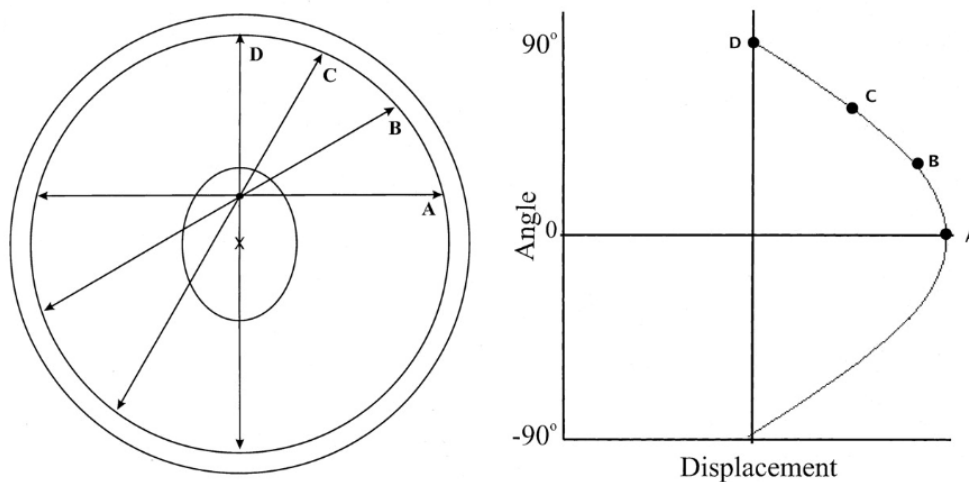
Figure 2.9: PET detector ring with a focus of interest in the middle with 4 lines of response passing through a point in that region of interest (left). The four lines of response are plotted in a sinogram [29]

Several events from different locations along the line of response all are detected by the same two detectors so they are stored in the same pixel. Therefore, for each coincidence event, the correspondent line of response is determined, the pixel in the sinogram is calculated and its value incremented. In the final sinogram, the value in the pixel represents the number of lines of response and therefore the number of coincidences, between the two detectors associated with that specific line of response.

3D PET sinogram are a combination of 2D direct sinograms and oblique sinograms. Therefore, the 3D PET data size increases rapidly with the number of scanner rings so in order to reduce the large size of

3D PET data, several adjacent lines of response are often combined in the axial direction. It is called axial mashing.

2.3.2   Arc Correction

Due to the curved nature of the detector ring, the lines of response passing near the centre will be more distant from each other than the ones on the edge of the field of view. Reconstruction algorithms assume that the lines of response are uniformly spaced so a correction must be made to compensate this disparity spacing between the different lines of response. It is called arc correction because it corrects the effect that is created by the fact that the detectors are arranjed an arc. The data is binned directly in lines of response with the same width. It is applied before reconstruction and is more important for larger objects where some lines of response are far from the centre [29].
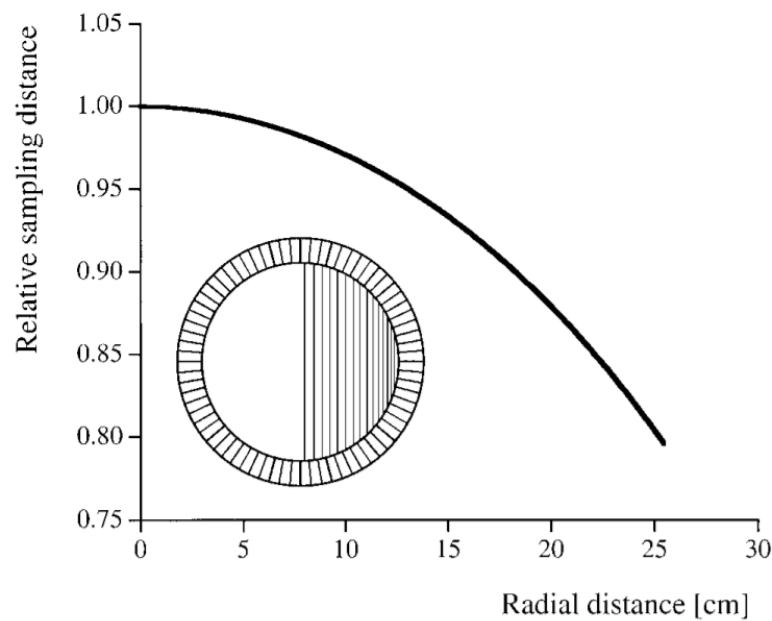
Figure 2.10: Change in the sampling distance as a function of the distance to the center of the scanner. The sampling distance at the centre of the field of view is set to 1 [30]

From Figure 2.10, it can be seen how the distance between consecutive lines of response (relative sampling distance on the graph) changes with the distance to the center of the scanner. In regions away from the center of the scanner, the distance between the lines of response decreases sharply. In whole-body scanners, geometric arc correction is relevant at radial distances larger than 10 cm [30].

2.3.3   Michelograms

Axial mashing of the data is an efficient way to reduce overall size and the noise in the data but reduces the axial spatial resolution. The Michelogram is a way of dealing with the axial sampling of the PET data and it was named after the Belgian scientist Christian Michel.

The Michelogram consists on the detector rings that belong to one side of the scanner plotted on the x-axis and the detector rings that are on the opposite side of the scanner plotted on the y-axis forming a 2D diagram. Each grid point corresponds to one ring pair and each oblique sinogram is represented by a line segment connecting two detector pairs, forming a plane [31]. Sinograms that have approximately the same axial angle are mashed together, creating segments. The positive segments are the sets with axial angle above zero and the negatives ones with axial angle bellow zero. If this strategy is used there is one important parameter that must be known: the span. The span determines the number of axial lines of response that will be combined together, being the sum of the number of cells on odd numbered planes plus the number of cells on even numbered planes (it can also be known by calculating the ring difference between two adjacent segments). The choice of span depends on the signal to noise ratio and on the radius of the field of view and it is usually between 3 and 9 [32].
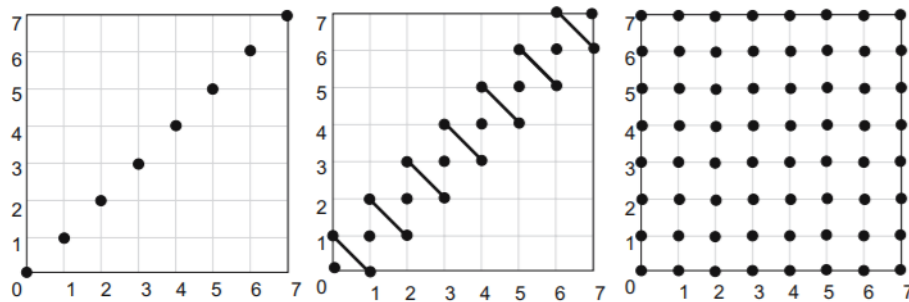
Figure 2.11: The graphical Michelogam shown for three different acquisition modes on a scanner with eight rings [33]

In Figure 2.11 we can see the created Michelograms for different different 2D data acquisitions using a PET scanner with 8 rings [32]. Figure 2.11 (a) there is a simple 2D acquisition with no inter-planes, the first plane defined is ring 0 in coincidence with the opposing detectors in the same ring 0 and it repeats for all of the rings. With this configuration, the data that is acquired results in 8 sinograms with axial sampling equal to the width of one detector. In Figure 2.11 (b) the same planes are acquired with the addition of a set of oblique planes formed between the rings with a ring difference of +1/-1 ring. Each one of these planes have twice the count rate compared with the adjacent plane which contains data from one ring only. This pattern is repeated for the rest of the rings resulting in 15 sinograms. This is a conventional 2D acquisition mode, resulting in almost twice the number of planes as the previous mode, improving axial sampling. Finally, Figure 2.11 (c) shows a 3D acquisition with each plane data being stored separately resulting in 64 sinograms.

2.4   Data correction

Data acquisition in PET is compromised by multiple effects. Thus, data correction is essential so that a high-quality image with low statistical noise can be obtained. The following sections will explain the basis of the different corrections used in PET.

2.4.1   Normalisation Correction

In the PET scanner, the crystals are closely arranged in adjacent rings to achieve high resolution images. Despite the closer crystal arrangements, there are gaps formed between the detector blocks and they can be visible in the reconstructed image. Because of this, detection sensitivity of a detector pair varies from pair to pair, resulting in non-uniform count rates along in principle equivalent detector pairs [34]. Information on these variations is required for the reconstruction of quantitative, artifact free, images. The method of correcting these variations is known as normalisation.

Normalisation is frequently accomplished by exposing all detector pairs to a positron emitter source with a very uniform activity concentration and distribution to grant uniform exposure of all lines of response. Data is collected for all detector pairs and normalisation factors are calculated for each pair by dividing the average of counts of all equivalent lines of response by the individual detector pair count. This process is known as direct normalisation. However, this has the disadvantage that scans need to be long enough to obtain adequate counts per line of response. The main problem of this method is that it requires accumulation of a large number of counts in order to achieve an acceptable statistical accuracy for each line of response.

2.4.2   Attenuation Correction

Attenuation can be described by Beer's law and it is the loss of detection of true coincidence events due to their absorption or scattering inside the body or detector. The annihilation photons interact with matter primarily through Compton interactions resulting in a decrease in photon energy (increase in wavelength) or through photoelectric effect. On reconstructing the PET image, this effect may produce more activity in the edges than in the center of the body due to various degrees of absorption of true events. This loss can result in up to a 90% of signal reduction in some regions of the human body and can lead to a more noisy and distorted image [35]. Attenuation depends on the photon energy, the electron density and atom number of the absorber. As attenuation is independent of the location of the annihilation along the line of response, it can be corrected by acquiring two scans of transmission, one without any object of study (black scan) and other with the object, providing the attenuation map.

2.4.3 Scatter Correction

Scatter is part of the attenuation phenomena, in which the photons deviate from their original directions and contribute to inappropriate lines of response. Therefore, they provide false information on the origin of source activity and affect the overall contrast of the PET image [9]. Usually the fraction of scattered events is very high (specially in 3D mode) but it depends on the object under study and the distribution of radioactivity. This results in false counts. The goal of the scatter correction is the removal of these false counts. The removal of scatter approximates a narrow beam geometry, which is the condition assumed for the attenuation correction. Therefore, it is important that scatter correction should be performed before correcting for attenuation.

Scatter contribution increases with the density and depth of body tissue, density of detector material, activity in the patient and energy window width of the PET system. There are many approaches to estimate and remove the scatter events from the detected events, such as analytical approach, methods based on energy window and simulation methods which can be done based on a model or using Monte Carlo methods.

2.4.4 Random correction

The PET system uses a timing window in order to detect photon pairs. However, two photons coming from two different annihilations can be detected within the same timing window. The detected random events provide misleading information related to the origin of activity and its spatial distribution, which results in an increase in background noise in the final image. Its probability of accounting in the prompts increases with the activity, therefore it is necessary to remove them in the process of imaging by estimating the fraction of random events in the prompt window.

The random coincidence rate increases with the square of activity, while the rate of true coincidences only increases linearly [10]. In order to correct random events two methods may be considered, one which uses a single time window and the other that uses two time windows, called the delayed time window.

2.5 Image Reconstruction

The basic role of image reconstruction is to convert the counts at projections measured at many different angles around the object, into a image that quantitatively reflects the distribution of positron-emitting atoms. There are two basic approaches to image reconstruction: the analytical approach which utilises the mathematics of computed tomography that relates line integral measurements to the activity distribution in the object. The second kind of reconstruction methods is an iterative approach. They model

the data collection process in a PET scanner and attempt, in a series of successive iterations, to find the image that is most consistent with the measured data.

Several iterative algorithms are proposed in the literature, being the Maximum Likelihood Expectation Maximization (MLEM) algorithm one of the standard iterative reconstruction methods [36]. It involves forward and backward projection of data in each iteration and takes around 30-100 iterations for a typical PET data which corresponds to a very high number of iterations needed to converge [37]. The Ordered Subsets Expectation Maximization (OSEM) algorithm was proposed to replace this slow algorithm. In this method, the entire data is partitioned to subsets depending on the angle and undergo iteration and the algorithm is accelerated with an increased number of subsets. Corrections can be included during the iterative process, for example, normalisation and attenuation correction are included in normalisation attenuation weighted OSEM, a method that is preferred in clinical practice because it shows less noise and artifacts.

Chapter 3

Monte Carlo Simulations

Monte Carlo methods, also called Monte Carlo experiments, are a broad class of computational algorithms that rely on repeated random sampling to obtain numerical results. The method involves solving problems, that might be deterministic in principle, through randomness. The Monte Carlo method was invented by scientists working on the atomic bomb in the 1940s, who named it after the city of Monaco which is famous for its casinos and games of chance. Since its introduction in World War II, Monte Carlo simulation has been used to model a variety of physical and conceptual systems.

A Monte Carlo simulation consists in a model that is able to simulate the behaviour of a system, based on a priori knowledge of the probabilities of occurrence of the different processes or interactions involved in the measurement chain. The various advantages of a Monte Carlo simulation are, rather than simply generating the final values, it provides probabilistic results to view how likely each outcome is and to see which input had the biggest effect on the bottom-line results [38].

Therefore, Monte Carlo is a valuable tool for forecasting any unknown procedures and can be applied to an incredibly diverse range of problems in science, engineering and business applications in virtually every industry. More specificaly, due to the stochastic nature of radiation emission and detection processes, the Monte Carlo method is of particular interest for medical physics in areas such as radiotherapy, radiation protection and nuclear medicine.

3.1   Random Number Generator

A pseudorandom number generator (PRNG), also known as a deterministic random bit generator (DRBG), is an algorithm for generating a sequence of numbers whose properties approximate the properties of

sequences of random numbers. The PRNG-generated sequence is not truly random, because it is completely determined by an initial value, called seed [39]. However, this seed may include truly random values. Although random sequences can be generated using hardware, pseudorandom number generators are important in practice for their speed in number generation and their reproducibility. PRNGs are central in applications such as simulations, electronic games and cryptography.

A good example of a PRNG is the Linear Congruential Method. The Linear Congruential Generator is the most common algorithm for generating pseudo-randomized numbers. In Equation 3.1 it can be seen an example of such algorithm [40]. To get started, the algorithm requires an initial seed, which must be provided by some means. For a given seed value, the simulation always produces the same set of numbers. A good deal of research has gone into pseudo-random number theory and nowadays modern algorithms for generating pseudo-random numbers are good enough so that the numbers look exactly like they are really random [41].

$$I_{n+1} = (aI_n + b) \mod (2^k) \tag{3.1}$$

In the equation above, a and b are constants and k is the integer word size of the computer. A series of a random number I_n is calculated from the first seed value I_0 as seen in Equation 3.1.

According to [40] the characteristics of PRNGs can be described as:

- **Efficient**: PRNG can produce many numbers in a short time therefore it is beneficial for applications that need many numbers

- **Deterministic**: A given sequence of numbers can be reproduced at a later date if the starting point in the sequence is known. This is important if there is a need to replay the same sequence of numbers again at a later stage

- **Periodic**: PRNGs are periodic, which means that the sequence will eventually repeat itself. While periodicity is hardly ever a desirable characteristic, modern PRNGs have a period that is so long that it can be ignored for most practical purposes

These characteristics make PRNGs suitable for applications where a large quantity of numbers is required and where it is useful that the same sequence can be replayed easily if needed. Popular examples of such applications are simulation and modelling applications. However, PRNGs are not suitable for applications where it is important that the numbers are really unpredictable, such as data encryption and gambling [41].

3.2   Applications in Nuclear Medicine

Monte Carlo methods have been applied to an incredibly diverse range of problems in science, engineering, finance and business applications. Specifically, Monte Carlo simulations are now an essential tool in emission tomography (SPECT and PET). These simulations have become a crucial tool for the development of emission tomography in various areas: designing of new medical devices, optimisation or acquisition protocols and the development of image reconstruction algorithms.

It is possible to design several types of radiation therapy treatment planning procedures using the Monte Carlo method. In those cases, the amount of dose generated from the source particle and the percentage absorbed by various parts of the body can be predicted. Therefore, right from the particle generation, tracking and interaction inside the source and measuring device, particle detection, data correction and all the other processes, which take place during the real-time measurement, can be simulated [42]. The most commonly used software for the Monte Carlo simulations is the GEANT4 Application for Tomographic Emission (GATE) code since it is appropriate for both SPECT and PET.

3.3   GEANT4 Simulation

For many years, the Monte Carlo codes dedicated to PET and SPECT had several limitations in terms of validation, accuracy and support therefore such codes were not enough to perform realistic simulations of emission tomography detector geometries. For example SimSet, one of the most powerful dedicated codes for PET and SPECT that existed back then, could not subdivide the detector ring in crystals and the gaps between them [43].

There was a need to have a Monte Carlo code capable of accommodating complex scanner geometry while retaining the comprehensive physics modelling abilities. Also these codes were not originally made for SPECT or PET being adapted to these imaging modalities, unlike the GATE software. Therefore, GATE appeared as a result of GEANT4 collaboration that developed a object-oriented software in C++ and it was initially developed to overcome limitations of existing codes [2].

3.4   GATE

As it was previously said, one of the most used programs to simulate PET data is the GATE software developed by the OpenGATE collaboration. It provides a complete simulation from decay to detection and its able to simulate numerous effects like dead time and decay kinetics. Several studies have been using this software for the past few year since it can assess design an performance parameters of PET

systems and identify potential effect on image quality before proceeding into the costly and time consuming process of hardware development.

Since it was made almost from scratch, GATE met some of the requirements that the other codes did not fulfil like being flexible to ensure that it could be possible to model any kind of SPECT and PET scanners and simulations. It also can simulate time-dependent processes and it is user-friendly enough for people who are not very familiar with Monte Carlo simulations [2].

3.4.1 Geometry

When defining the scanner geometry, the geometrical hierarchy of the scanner components must be taken into account so that the particles generated that interact with the detectors, can be processed and produce a realistic output. Most of PET scanners have similar geometry arrangement: possess one or more rings, each ring is divided in r sectors, each r sector is decided in modules, each module is divided in submodules and each submodule is divided in crystals. The number of hierarchy structures varies between the scanners (it is not always 5 like the example, it can be more or less). Usually a component is inserted and then its repetition is set: its length and number or repetitions in each direction (as seen in the example for the crystal shown below). The material also needs to be always defined for every component.

/gate/submodule/daughters/name crystal
/gate/submodule/daughters/insert box
/gate/crystal/geometry/setXLength 25. mm
/gate/crystal/geometry/setYLength 3.95 mm
/gate/crystal/geometry/setZLength 5.3 mm
/gate/crystal/setMaterial LSO
/gate/crystal/repeaters/insert cubicArray
/gate/crystal/cubicArray/setRepeatNumberX 1
/gate/crystal/cubicArray/setRepeatNumberY 4
/gate/crystal/cubicArray/setRepeatNumberZ 3
/gate/crystal/cubicArray/setRepeatVector 0. 3.95 5.3 mm

In this example, the crystal is defined. Firstly, the crystal is inserted in the existing geometry. Afterwards, its length and material are defined. In the end, the number of times the it is repeated, in each direction, and the repeating vector are also defined.

3.4.2   Phantom

A phantom is a specially designed object that is scanned or imaged in the field of medical imaging to evaluate, analyse, and tune the performance of various medical imaging devices. In most cases, they are modeled to be similar to human tissues or organs in order to study response to irradiation. A phantom is more readily available and provides more consistent results than the use of a living subject and avoids the liability of putting a living organism to radiological risk.

GATE is able to read digital phantom or clinic data stored in various image file formats so as to allow users to read attenuation maps or emission data from these voxelized phantoms and sources. To read in voxelized phantom, GATE requires a text file for the description of materials, a 3D image stored in one of the following formats: ASCII, Interfile, Analyze, MetaImage and DICOM and a text file for the description of activity levels.

3.4.3   Sources

The sources are usually defined inside the phantom. The properties to consider while defining a source are the shape (point, line and plane), activity, position, movement during the simulation, energy of the emitted particle and the type of particle simulated. GATE offers a variety of sources like "Fluor18" and "backtoback". The activity is easily defined with a value unless it is a voxelized phantom (that contains a voxelized source). In that case, as mentioned before, GATE requires a text file with the description of the activity levels in which each voxel of the grayscale image is converted into an actual activity value using a range translation table.

3.4.4   Digitizer

The digitizer consists in a chain of processing modules that takes a list of hits from the sensitive detectors and transforms them into pulses that are referred to as singles [2]. The processing elements are explained in the following sections.

3.4.4.1   Adder

The particles generated from the source undergo interaction with the detector crystal and sometimes multiple interactions can happen within the same crystal. For such cases, the electronics at crystal level do not have sufficient energy or time resolution to distinguish the different interactions taking place inside a crystal. Therefore, the adder module sums up the deposited energy of these interactions within a crystal to yield a pulse. If a particle interacts in several crystals, the hit adder will generate a list of pulses, one for each crystal.

3.4.4.2   Readout

In a PET detector, the basic idea is that each crystal is read by an individual photo-detector, but the readout segmentation often differs from its basic geometrical structures. The readout segmentation or readout module is an artificial geometry that is associated with a group of sensitive detectors and reads the pulses produced from the adder module.

3.4.4.3   Energy Window

Upper and lower energy thresholds are set for several energy windows by using multiple processor chains. These thresholds are applied using a sigmoid function. The thresholder and upholder module help discarding low and high energy pulses by setting an energy window, and users have the freedom to set these input parameters. By setting an appropriate value to these parameters, it is possible to simulate the behaviour of real scanners by predicting accurate scatter fraction and count rate performances.

3.4.4.4   Coincidence Sorter

At the end of the digitizer chain, a coincidence sorter is added to check the singles list and if two or more singles are found within a user defined coincidence window, it is considered as a coincidence event. Each single is stored with its event number. If the event numbers are different, it is considered a random coincidence. In order to differentiate true from scatter coincidences, a Compton scatter flag is used.

The minimum sector difference is also defined in this section and represents the difference between the r sector numbers where singles are detected. Only if the 2 singles are separated by a number of R sectors greater than or equal to the minSectorDifference value, they are considered to form a good pair, otherwise the coincidence event will be rejected.

The temporal resolution module introduces a Gaussian blurring in the time domain. It works in the same manner as the energy blurring module but with time instead of energy.

The final parameter is the multiple policy which comes into picture when more than two singles are found to be in coincidence. Therefore, GATE allows nine different rules to choose the appropriate coincidence event and the default policy is keepAllAreGoods.

3.5   TOF GATE

A great advantage of Monte Carlo simulations is the possibility to model time-dependent phenomena like TOF and others. The Monte Carlo codes can do that by performing numerous simulations just changing the input data or the detector description between them. Most of the codes that existed before

GATE could only model some time-dependent phenomena but GATE brought the option to model even more phenomena. It can model detector motion, time–activity curves in different physiological regions, radioactive decay, TOF PET and physiological motions. [43].

3.6   ROOT

The output data from GATE simulation is analysed using the ROOT software system, an object-oriented program and library developed by the European Organization for Nuclear Research (CERN). CERN originally developed ROOT to analyse high energy physics data but due to its prominent features such as the ability to deal with big data processing, statistical analysis, visualisation and storage, it is also being used in other scientific fields. One of the advantages of ROOT is the fact that it provides a data structure called TTree which makes it faster to access enormous amounts of data.

Chapter 4

Simulation Approaches with BrainPET

The main focus of this chapter is to compare two different methods to obtain the coincidence data necessary to obtain sinograms so that images can be reconstruct from simulations with different time resolutions. In this chapter, the reader is presented with a more time costly method using GATE and a script made by Paola Solevi from Otto-von-Guericke-Universität Magdeburg which is much faster. A description of the performed simulations, the definition of some parameters and comparison between both methods will be presented here.

4.1 Simulation

The simulations were performed using the Siemens BrainPET scanner parameters. In the next sections, all the scanner parameters are displayed and they were all defined according to the real BrainPET scanner located in the Forschungszentrum Julich Institute of Neuroscience and Medicine-4 (INM-4) as shown in Figure 4.1. Due to the fact that this simulations require a considerable computational power, they were all performed on "mrcluster", a INM-4 cluster.

4.1.1 Geometry

The BrainPET was the first prototype of an MR-compatible PET scanner for human imaging. Four prototypes have been installed between 2006 and 2010 at: Tübingen (University Hospital), Boston (Massachusetts General Hospital), Jülich (Forschungszentrum Juelich) and Atlanta (Emory University).
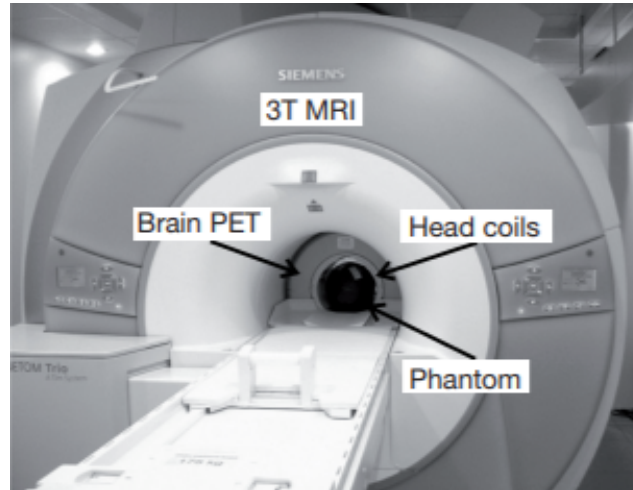
Figure 4.1: The 3TMR BrainPET as installed in the Forschungszentrum Jülich taken from [44]

The BrainPET is one of the components of the hybrid 3T-BrainPET scanner that enables simultaneous PET/MR imaging of the human brain and is located in Forschungszentrum Julich more specifically in the INM-4. The scanner is a Siemens 3 Tesla Tim System MAGNETOM Trio and the BrainPET is operated inside the bore of the scanner. Without the BrainPET insert, the MAGNETOM Trio can be operated as a standard scanner so one of the advantages of this scanner is the fact that the two components can be used individually [45].

The BrainPET consists in a compact cylinder with 72 cm of length, an outer diameter of 60 cm and inner diameter of 36 cm [46]. The axial field of view is 19.2 cm and the transaxial field of view is 31.4 cm. It consists of 32 detector cassettes and due to the geometric constraints in the number of electronic channels provided by the QuickSilver architecture (maximum 192 channels) the cassettes have a 6 mm gap between them in the same ring [47]. Each cassette has 6 detector blocks which are also separated by gaps of 2.5 mm. These detector blocks consist of 12 x 12 array of LSO crystals with and individual size of 2.5 x 2.5 x 20 mm^3. The crystals are coupled to 3 x 3 array of APDs each with an area of 5 x 5 mm^2.

To minimize the interference with the MR radio-frequency field, each cassette was shielded with 10 µm of copper [48]. Additionally each detector has a high voltage board that supplies 500 V to the APDs, a board with a 10-channel charge sensitive pre-amplifier application-specific integrated circuit (ASIC), a pulse-shaping and mapping board and an ASIC output driver board [45].

4.1.2 Phantom

One of the phantoms used in this study was the Hoffman Brain phantom (Figure 4.2). The purpose of the voxelized phantoms is the use of digital phantoms or patient data inhomogeneous anthropomorphic attenuation maps and therefore get realistic acquisitions [49]. Several files are necessary to describe and simulate a voxelized phantom: an interfile image associated with a 3D raw image, a range translator and

an activity translator table (in order to read the voxelized source).

In order to import a digital phantom as a voxelized geometry, GATE uses a navigator algorithm that tracks particles from voxel to voxel. From the several navigators available the "ImageRegularParametrisedVolume" was the one used in this study.
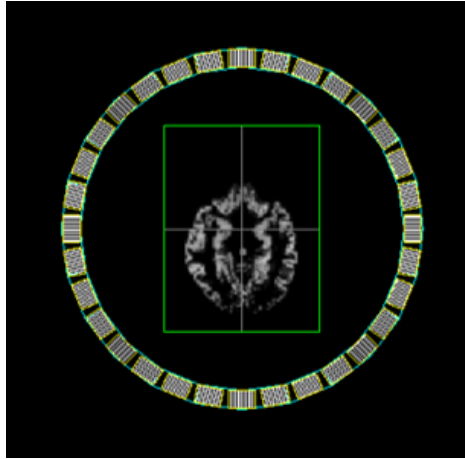
Figure 4.2: Transaxial view of the Hoffman Brain Phantom obtained with GATE's visualisation tool

If the materials are already defined in the "GateMaterials.db" file, their properties are assigned to each voxel using a range translator. This translator reads a materials table that has each material associated with a range of values. A material is associated to a voxel if the voxel value is within a specific material range.

4.1.3 Digitizer

After defining the phantom, the digitizer module is the next step in the simulation. The specifications include the energy resolution, the energy thresholds and the coincidence sorter that includes the coincidence time window, the minimum sector difference and the time resolution. These values are all included on Table 4.1.

Table 4.1: Digitizer specifications of the BrainPET

Energy resolution at 511 KeV	22% at FWHM
Energy threshold	420 – 600 KeV
Coincidence Time Window	12 ns
Minimum Sector Difference	6/7 (depending on the simulation)
Time Resolution at FWHM	5.6 ns

4.1.4 Source

In order to read voxelized sources, GATE needs a text file with a description of the activity levels that is read with the help of a range translator. This file has a table with intervals each one of them associated with a predefined activity value. Each voxel of the grayscale image is associated to an activity value if the value in the voxel is within an interval of that activity "level".

The source type also needs to be defined. From the multiple options that GATE offers, this study used a back-to-back source that is usually used in PET studies since it produces two annihilation photons at 180 degrees. Some parameters need to be specified in order to define the source: the particle (gamma), the energy type (Mono), the energy value (0.511 MeV) and the emission angle (isotropic).

4.1.5 Random Generator

As a Monte Carlo tool, GATE needs a random generator that can be chosen from multiple options. In this study Mersenne Twister was chosen since it is the default generator used in PET simulations. The generator seed also needs to be defined and in this case the option chosen was "default". In this case, the default CLHEP (Class Library for High Energy Physics) internal seed is taken so the value is always the same.

4.2 Time of Flight

TOF-PET is a technique that tries to identify approximately the position of annihilation along the line of response by measuring the difference in the arrival times of the photons. In GATE it is done by adding two lines to the coincidence sorter:

/gate/digitizer/Singles/insert timeResolution

/gate/digitizer/Singles/timeResolution/setTimeResolution 5.0 ns

Using the parameters described in the previous section, two simulations were done: one without time resolution and another with time resolution. From the simulation ROOT output, a plot containing the arrival time difference of the photons in each coincidence can be obtained for both simulations. This plots (for the true coincidences) can be seen on Figure 4.3.

In the simulation without time resolution, the plot that is obtained is just the difference between the arrival times of the photons. On the other hand, the plot that comes from the simulation with time resolution is obtained by blurring the gaussian with the difference in the arrival times with the gaussian of the time resolution.
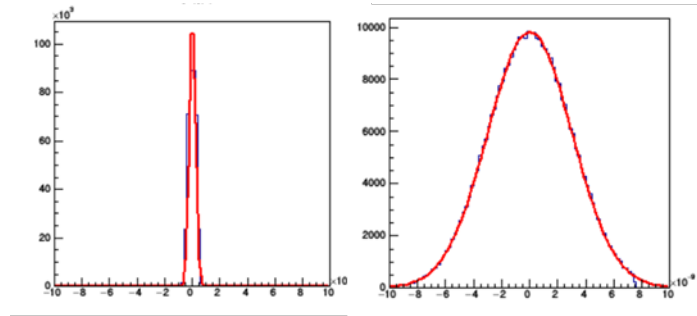
Figure 4.3: Arrival time difference in true coincidences without time resolution (left) and with time resolution (right)

From the plots showed on Figure 4.3, it is clear that with the introduction of time resolution the values of the arrival time difference peak at the same position and the values are more spread.

4.3   Paola Solevi's Script

In the GATE simulation, time resolution is applied during the simulation but it takes several hours. However, Paola Solevi from Otto-von-Guericke-Universität Magdeburg developed a script that applies a time blurring to the already existing data, i.e., data without time resolution. After applying the time blurring to each single, the number of each type of coincidences is calculated since the script also contains a coincidence sorter. This script usually takes less than one minute to run.

In order to run the script, a ROOT file from the simulation performed without the time resolution is needed. This simulation needs to have the same characteristics as the one we are trying to analyse like the geometry, phantom, source and digitizer specifications. Other inputs for this script include the number of singles and coincidence time window of the simulation (with no time resolution) and the value of the time resolution intended for the new simulation. In order to obtain the correct results it is important to correctly declare the value of the minimum sector difference (chapter intro) since it minimises the error in the final results.

The outputs of the script are a root file, that can be analysed just like a usual root file obtained with GATE, and the number and percentage of each type of coincidence saved in a separate file.

In essence, this script allows us to do a simulation with time resolution without having to do the whole simulation in GATE where it would take hours instead of seconds. One of the advantages is in the studies where numerous time resolutions are being tested so there is no need to take hours in order to do various simulations and instead just running the script for each one of those time resolutions. The downside is that the root file from a simulation without time resolution is always needed so the simulation without time resolution has to be always performed since it is one of the inputs and contains the number of singles and coincidence time window that are also inputs for the script.

One of the objectives of this study was to find out how some parameters must be defined and changed from the base script so that it can run properly and be a viable replacement for GATE.

4.4 Comparison between two different strategies for multiple coincidences

In this section, the number of each type of coincidences obtained with the GATE simulation is going to be compared with the one obtained with Paola's script and the differences that exist when using distinct policies for the multiple coincidences. At the end of this section the best policy is defined in order to proceed with other analysis.

4.4.1 Methods and Results

When more than two photons are detected in different detectors within the coincidence time window it is called a multiple coincidence. Several approaches can be implemented and GATE offers 9 different rules to be applied when a situation like this happens. The multiples policy that was used at first was "killAllIfMultipleGoods": if more than one pair is good, it is considered a multiple event and therefore all events are discarded.

Two simulations were performed using this policy, one without time resolution and another with time resolution. The parameters used were the ones described in the previous section (Section 4.1) and both simulation were set to 10 seconds. The number of each type of coincidences can be seen in Table 4.2 for simulations with and without time resolution.

Table 4.2: Number of each type of coincidences obtained in a simulation done with "killAllIfMultipleGoods" defined as multiples policy, with and without time resolution using two different methods

	Method	**Total Coincidences**	**Random**	**Scatter**	**True**
Without time resolution	Time blurring	286967	3660	59549	223758
	GATE simulation	283862	2457	58421	222984
Difference (%)		-1.09	-48.96	-1.93	-0.35
With time resolution	Time blurring	286669	3958	59502	223209
	GATE simulation	283380	2588	58487	222305
Difference (%)		-1.16	-52.94	-1.74	-0.41

From the Table 4.2 it is possible to observe that the total number of coincidences is similar in the two methods. Also, the number of scatter and true coincidences is almost identical (differences below 2%). However, the number of random coincidences detected is lower on the GATE simulation comparing to Paola's script (48.96% less in the simulation without time resolution and 52.94% in the simulation with

time resolution).

Since Paola's script did not specify the multiples policy that was meant to be used, changing the policy used in the GATE simulations to "takeAllGoods" was the approach chosen in order to test if this was the reason for the discrepancy in the number of random coincidences. When using this policy, all the good pairs are considered events, raising the number of randoms. The number of each type of coincidences obtained with each method and using the "takeAllGoods" as multiples policy in the GATE simulations can be seen in Table 4.3, for simulations with and without time resolution.

Table 4.3: Number of each type of coincidences obtained in a simulation done with "takeAllGoods" defined as multiples policy, with and without time resolution using two different methods

	Method	**Total Coincidences**	**Random**	**Scatter**	**True**
Without	Time blurring	286967	3660	59549	223758
time resolution	GATE simulation	287035	4201	58713	224121
Difference (%)		0.02	12.87	-2.31	0.16
With	Time blurring	286669	3958	59502	223209
time resolution	GATE simulation	286054	4049	58738	223267
Difference (%)		-0.21	2.25	-1.30	0.03

From the table above it is possible to observe that the total number of coincidences is similar in the two methods. The number of scatter and true coincidences also remains identical. In the simulation with time resolution, the number of random coincidences is very similar between the two methods and a great improvement from the previous values obtained with "killAllIfMultipleGoods" policy. In the simulation without time resolution, there is still a considerable difference between the values of the two methods: the number of random coincidences obtained is almost 13% superior to the value obtained with Paola's script. However, since the main focus of this study and script are the simulations with time resolution, this value can be ignored since it is not important.

In order to test if this behaviour would remain the same using different values for the time resolution, 5 simulations were done for each one of the multiples policies mentioned before. These simulations had different time resolution values: the scanner original value 5.6 ns and 4, 4.5, 5 and 6 ns as the other values. The other scanner parameters remained the same (Section 4.1), except for the coincidence time window. According to [24] the value for the coincidence time window should be twice the value of the time resolution of the scanner. Because of this, the coincidence time window was adjusted to double the value of the time resolution in each one of the simulations instead of the 12 ns value of the BrainPET scanner. The simulation time was 10 s for each one of the cases with time resolution and for the simulation without time resolution. The different events were obtained with GATE and with Paola's script using the data from the simulation without time resolution. Since the main difference between the two policies was the number of random coincidences, the main focus was on the difference between the values obtained with each methods with the two different policies. Therefore, plots were obtained showing

the values achieved with both methods for each multiples policy and they are displayed on Figure 4.4.
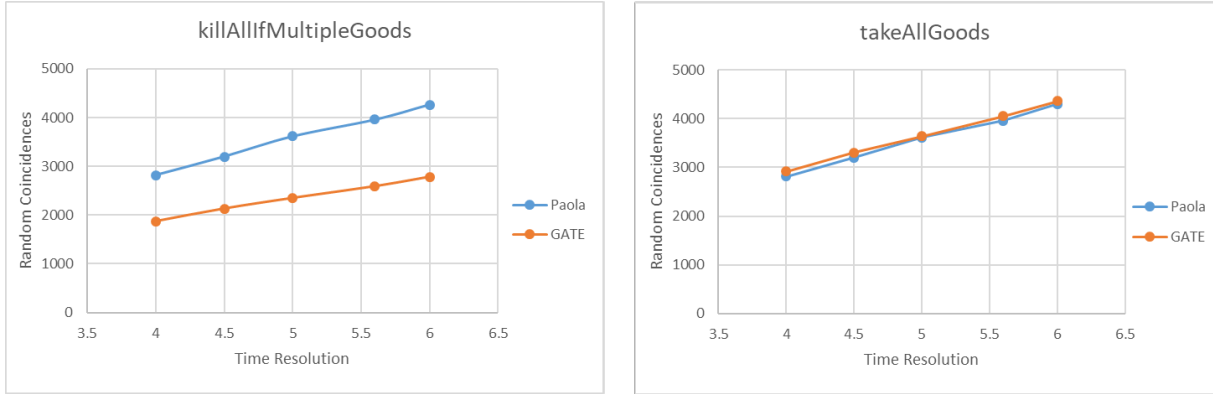

Figure 4.4: Number of random coincidences obtained in simulations with different time resolutions using two different methods (Paola's script and GATE simulaltion) and two different multiples policy: "killAllIfMultipleGoods" (left) and "takeAllGoods" (right)

From the plots in Figure 4.4, it can be seen that the difference between the values obtained with each method in simulations that used the "killAllIfMultipleGoods" policy, remains considerable large even though the time resolution was changed. It also can be seen that the difference between the absolute values is larger in simulations with an higher value for the time resolution (950 for the simulation with 4 ns as time resolution and 1486 for the simulation with a time resolution of 6 ns).

When we look at the plot containing the information regarding the simulation performed with the "takeAll-Goods" multiples policy, we can see the proximity between the number of random coincidences obtained with both methods. Specifically, for the simulation performed with a time resolution of 5 ns the difference in the number of random coincidences is less than 1%.

It is also important to refer that the number of random coincidences obtained with GATE is always higher than the number achieved with Paola's script, even though the difference is small.

4.4.2   Discussion

Looking at the results obtained in the previous section, it can be seen the advantage of using "takeAll-Goods" as multiples policy instead of "killAllIfMultipleGoods". Even though the time resolution value was changed, the difference in the number of random coincidences for "killAllIfMultipleGoods" policy remained the same so it can be considered a pattern for that specific policy and therefore it is not the correct one to use with Paola's script. However, for "takeAllGoods" the values are always very similar between the two methods. Therefore, these results show the viability of applying a time blurring after the simulation without the time resolution if the multiples policy chosen is "takeAllGoods".
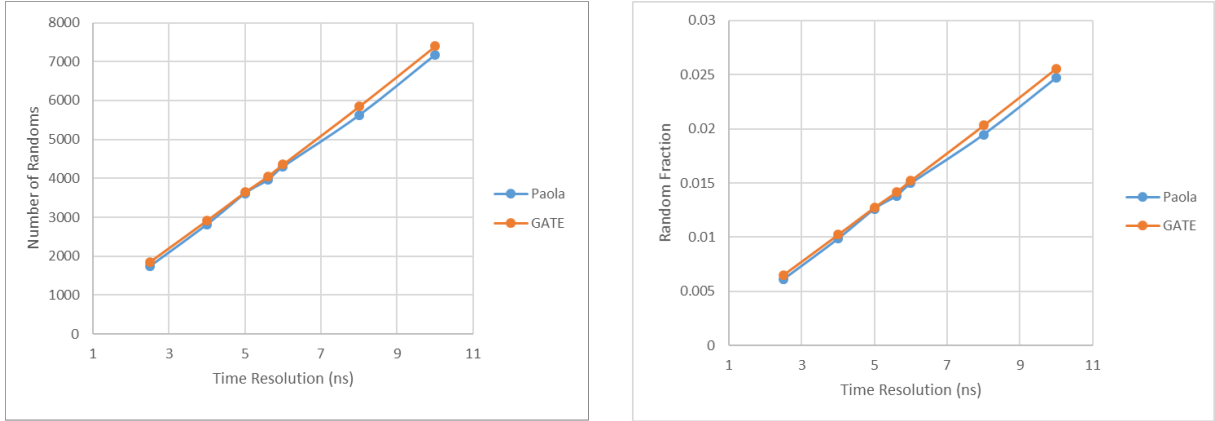
Figure 4.5: Number of random coincidences (left) and random fraction (right) obtained from simulations with different values for the time resolution, with two different methods (Paola's Script and GATE)

4.5 Effect of time resolution on different simulation outputs

After defining the multiples policy used in the simulation ("takeAllGoods"), the outputs obtained need to be analysed according to the time resolution. The simulations were performed with the parameters mentioned in Section 4.1, changing only the time resolution (2.5, 4, 5, 5.6, 6, 8 and 10 ns) and the coincidence time window to double the value of the time resolution.

4.5.1 Randoms and random fraction

As previously mentioned in Section 2.1.4.3, the rate of random coincidences is proportional to the coincidence time window. Therefore, a small coincidence time window helps reducing the number of random coincidences. However, the coincidence time window needs to be large enough to allow true events to be accepted. Having this into consideration, [24] states that the value for the coincidence time window should be twice the value of the time resolution of the scanner in order to have the optimal value between the number of random and true coincidences.

In order to study the behaviour of the number of random coincidences and random fraction depending on the time resolution (and coincidence time window) plots were obtained and are displayed on Figure 4.5.

Figure 4.5 shows how the number of randoms and the random fraction changes with the value of the time resolution obtained with the two different methods. It is possible to see that the change in the number of random coincidences is as expected: it gets lower with the time resolution (and smaller window). Additionally it is possible to observe the similarity between the number of random coincidences obtained with the two different methods.

It can also be seen that the fraction of random coincidences slightly increases with the value of the time

resolution and the values are very similar between the two methods. However, the values are around 0.1-0.2 which are considered low comparing to the usual values that are around 0.35. This can be due to the fact that the phantom used had low activity so it did not produce realistic results.

4.5.2 Scatter and scatter fraction

Assessment of PET scanner performance is mandatory to prevent image artifacts and one of the parameters used to analyse it is the scatter fraction. As previously mentioned in Equation 2.6, the scatter fraction is equal to the number of scatter coincidences divided by the sum of this type of coincidences with the number of true coincidences. The number of scatter coincidences and the scatter fraction obtained with two different methods depending on different time resolutions is shown on Figure 4.6.
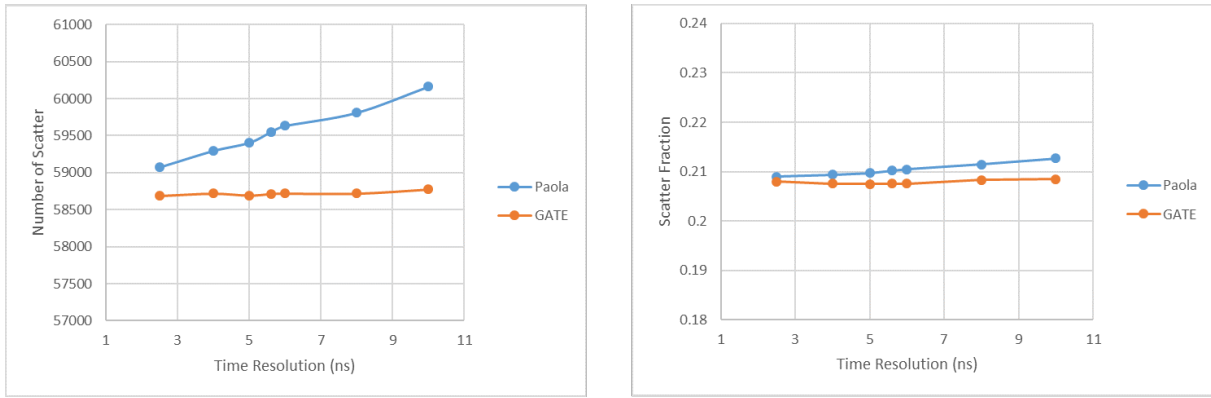
Figure 4.6: Number of scatter coincidences (left) and scatter fraction (right) obtained from simulations with different values for the time resolution, with two different methods (Paola's Script and GATE)

From Figure 4.6 it can be observed that the number of scatter coincidences goes slightly increases when the time resolution is larger. This is due to the coincidence time window being larger and accepting an higher number of coincidences since the scatter are only affected by the activity distribution, object and camera geometry which remained the same in every simulation.

In Figure 4.6 there is also another plot displaying the scatter fraction. It can be seen that the scatter fraction remains almost the same throughout all the different time resolutions, having a value around 21%. This is a little below the usual value that is around 30% (Section 2.1.4.2). This may be due to the fact that in the phantom used, the voxelized Brain phantom, the skull was not considered in the attenuation values lowering the total number of scatter coincidences.

4.5.3   Discussion

From the results obtained in the previous section, it can be seen the similarity between the values obtained with the two different methods in almost all parameters. The difference between them is always a small percentage excluding the number of scatter coincidences. However, the difference in the number of scatter coincidences is small and can be explained by the larger window that is used in higher time resolution values.

Overall, the script produces similar results to the ones obtained in GATE so it can be considered an option to replace the GATE simulations saving a lot of time. It is important to notice that the simulation with no time resolution needs to be always done in order to have the script inputs.

4.6   Simulation with a more realistic phantom

The results from the previous section show a low percentage of random and scatter coincidences, very different from the values usually obtained in scanners. Therefore, in order to obtain more realistic values, a new phantom was simulated. This phantom was also a voxelized brain phantom but unlike the previous one, this simulated the skull and had higher activity. It is displayed on Figure 4.7.

Like the previous voxelized phantom, this phantom had multiple files necessary to describe it: a interfile associated with a 3D raw image (accompanied with a header), a range translator table and an activity translator table.
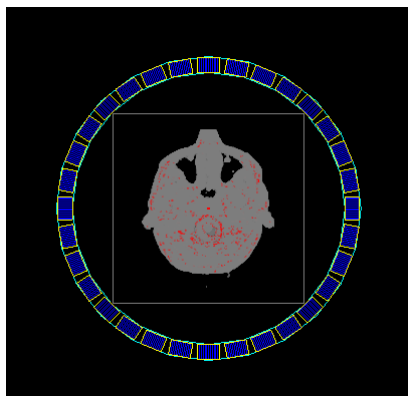
Figure 4.7: Transaxial view of the Voxelized Brain Phantom obtained with GATE's visualization tool

4.6.1   Simulation

The simulations were performed with the same parameters that were described before for the geometry, digitizer and random generator. Taking into account the results that were previously obtained, the multiples policy chosen was "takeAllGoods". The approach in which the coincidence time window is double

the value of the time resolution was not adopted here so the coincidence time window was defined as 12 ns the value that exists in the BrainPET scanner. In this study, the only variable between the simulations is the time resolution.

## 4.6.2   Results

The study about the previous phantom included an analysis of each type of coincidences also including the random and scatter fractions obtained from the simulations with different time resolutions and with the two different methods (Paola's script and GATE simulation). The same approach was used here.

Therefore, in order to study the behaviour of the number of random coincidences and random fraction depending on the time resolution were plotted and displayed on Figure 4.8.

Figure 4.8: Number of random coincidences (left) and random fraction (right) obtained from simulations with different values for the time resolution, with two different methods (Paola's Script and GATE)

The left plot on Figure 4.8 shows the number of random coincidences obtained with the two different methods. As mentioned before, the number of randoms decreases when the window is smaller. However in this study, the window remains the same in all simulations. Also, the number of randoms decreases with time resolution. Using Paola's script, the number of random coincidences follows this behaviour: the higher the value for the time resolution, the higher the number of coincidences. However, that does not apply for the GATE simulation. The number of random coincidences decreases when the time resolution value increases. Although not a big increase, it is still noticeable and against the expected behaviour.

The right plot on Figure 4.8 shows the random fraction obtained with the two different methods. The results show that the random fraction stays more or less the same in the GATE simulations (around 0.36) and between 0.35 and 0.38 using Paola's script.

The behaviour of the number of scatter coincidences and scatter fraction depending on the time resolution (and coincidence time window) also needs to be analysed and is displayed on Figure 4.9.
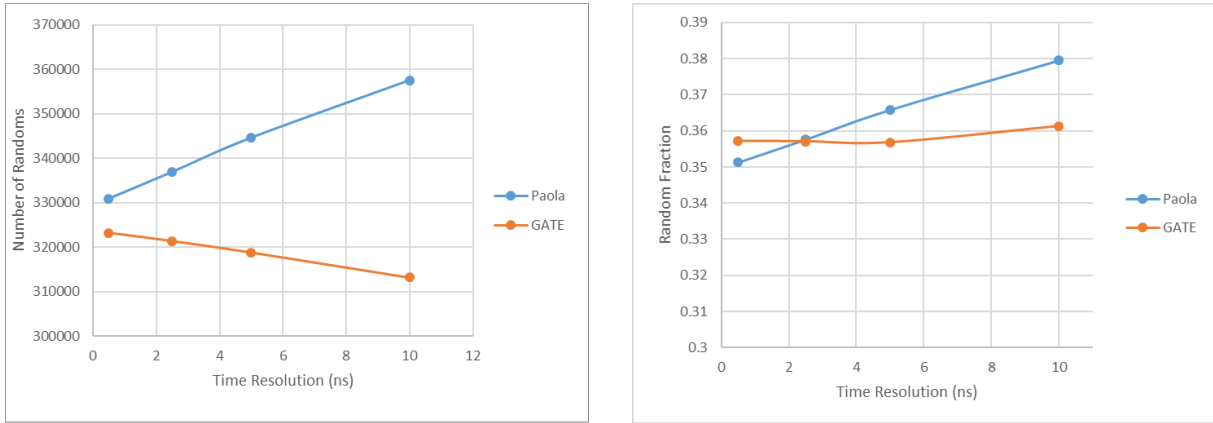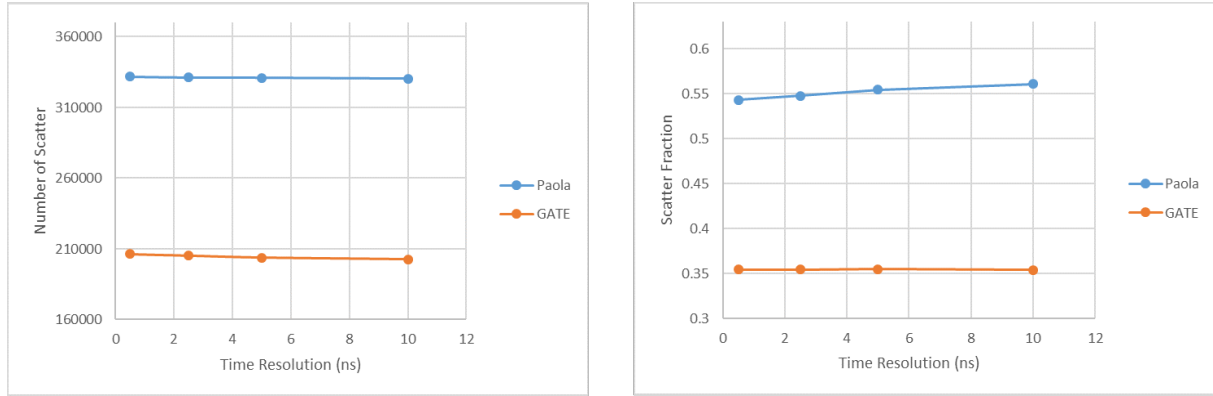

Figure 4.9: Number of scatter coincidences (left) and scatter fraction (right) obtained from simulations with different values for the time resolution, with two different methods (Paola's Script and GATE)

From Figure 4.9 it can be observed that the number of scatter coincidences is almost the same throughout all the time resolution values. However, ther is a big difference between the values obtained from the two methods: the ones obtained with Paola's Script are much higher than the ones obtained with GATE.

In Figure 4.9 there is also another plot displaying the scatter fraction. It can be seen that the scatter fraction is similar throughout all the values for the time resolution but different between the two methods. This is expected since a big difference between the number of scatter coincidences between the two methods was observed before. The values obtained with Paola's Script are really high comparing with the values that usually happen on the scanners (below 40% as seen on Section 2.1.4.2).

4.6.3 Discussion

When analysing the values obtained with this last phantom, it can be see that even though the number and percentage of random coincidences is similar to the ones that usually happen in the scanners, the number of random coincidences obtained in the GATE simulation decreases when the value or the time resolution is higher which is not the expected behaviour. The values obtained for the scatter fractions were also very different between the two methods.

It is important to notice that with this phantom the coincidence time window was not changed to double the value of the time resolution and it may had an impact on the results that were obtained. It can also be a parameter in Paola's script that was not taken in consideration but should have. The amount of problems that appeared with this phantom that did not exist in the previous phantom may be a signal of some kind of problem with this phantom so one of the tests that may be done is using an Hoffman Brain Phantom with higher activity.

Chapter 5

Simulation and Reconstruction of GE Signa PET-MR Scanner Images

The main focus of this chapter is the development of a pipeline method to reconstruct images from simulations done with the GE Signa PET-MR scanner characteristics. The method includes the description of the simulations performed in GATE, the data transformation from GATE to MATLAB, the calculation of the uncorrected sinograms, the process done in order to do the arc correction and to obtain the correct sinograms, the steps done to obtain the final normalisation file and all the reconstruction processes performed in order to obtain images are also explained. In the end of this chapter, reconstructed images (of two phantoms) with and without corrections are presented in order to evaluate the developed method.

5.1   Scanner

The GE Signa is a whole body integrated TOF-PET-MR scanner from GE Healthcare that allows simultaneous PET and MR imaging with sub 400 ps coincidence time resolution [50]. It combines the power of 3 T MRI alongside an integrated PET with exceptional quantitative count rate accuracy. The result is delivery of a three times higher sensitivity scanner than previous generations of PET technology. The simultaneous acquisition of PET and MR data enables new opportunities for clinicians: MR allows the imaging of soft tissue as well as functional and morphological details and PET enables clinicians to visualise cellular activity and metabolism. Since it provides simultaneous imaging, the time spent by the patient in the scanner is also reduced.

It uses SiPM that have high gain which allows time of flight reconstruction. The time of flight information

is important to determine the attenuation map in the absence of a transmission map. The combination between these two image modalities has some challenges (for example photon attenuation correction) but also offers new opportunities like motion correction and MR guided PET image reconstruction [51]. In order to study these issues, it is important to have a realistic numerical model of the scanner and its components. For the past few years, Monte Carlo simulations have been used to model and study the performance of different scanners, including hybrid PET-MR. GATE provides the tools to create a realistic model with Monte Carlo simulations.

The design of the integrated SIGNA PET-MR was based on the 3T MR750w MR scanner (GE Healthcare), a whole body MRI system with a 70 cm patient bore. The Radiofrequency (RF) body coil and RF shield were redesigned in order to accommodate the PET detector ring, and to shield it from the RF transmit power. The PET detector was placed between the RF shield and the gradient coil, with the RF body coil inside the PET ring [52].

Despite the complementary imaging capabilities of PET and MRI, their respective hardware tends to be incompatible due to mutual interference so the PET system needs to be designed so it can operate in the MR environment. This environment creates challenges of lack of space, strong magnetic field, thermal stress, vibrations, and large electromagnetic fields (from RF and gradients). While being robust to these environmental stresses, the PET system needs to be electromagnetically quiet to prevent interference with the low level signal detected by the MR. To achieve good electromagnetic isolation, a multi-layered approach to shielding was used. The only electrical connection to each module is through a double-shielded (braid plus foil) cable that carries power and timing clock over twisted pair wiring; all other communication and control takes place over dual optical fibers [52].

5.2 Simulation

In order to obtain the data needed to get cylinder images, several simulation parameters had to be defined so that the simulation could be performed. All simulations were performed using GATE software and the parameters used are described in the next sections.

5.2.1 Geometry

In order to perform the simulation of the GE Signa PET-MR scanner, the first step was to define the geometry by reproducing the real scanner geometry in the GATE macro. The specifications of the scanner were published in [51].

The field of view is 64.5 cm in the trans-axial direction and 25 cm in the axial direction. The scanner
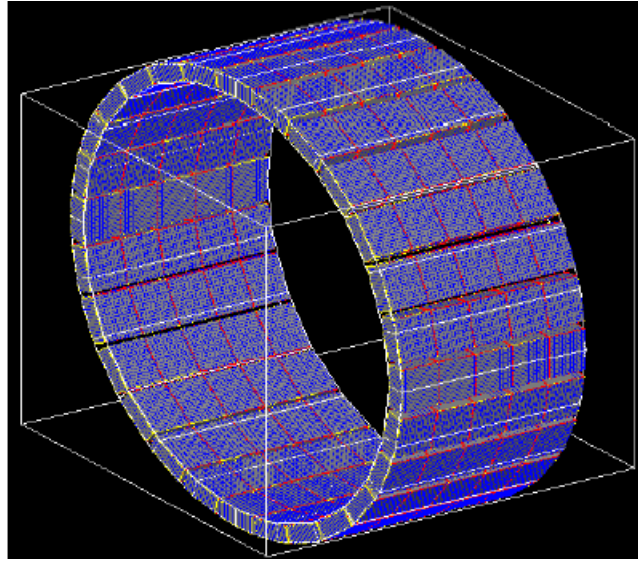
Figure 5.1: GE Signa PET-MR scanner geometry reproduced in GATE.

is made of 28 R Sectors disposed in a cylinder. Each of these R sectors is composed by 5 modules placed in the axial direction. On the other hand, each module has 4 submodules in the trans-axial and 3 submodules in the axial direction. Lastly, each submodule is composed by 4 LYSO crystals in the trans-axial direction and 3 LYSO crystals in the axial direction. A single crystal has 25 mm of length, 3.95 mm in the trans-axial direction and 5.3 mm in the axial direction. In total, the scanner has 45 rings with 448 crystals each bringing the total number of crystals to 20160. The final geometry reproduced in GATE is in Figure 5.1.

Since only the dimensions for the R Sector and for the crystals were known, calculations had to be done in order to know the dimensions of the parts in between (modules and submodules) and the gaps that exist between the different constitutes of the scanner. The final dimensions of every part (already including the gaps) are on Table 5.1 along with the dimensions already referred before. The detailed description alongside 3D drawings is in Figure 6.2 on the Appendix.

Table 5.1: Dimensions (in mm, including the gaps) of each component of the scanner and also the number and arrangement of the smaller parts within each component, i.e., the number and arrangement of the crystals within the submodule, the number and arrangement of the submodules within a module, etc.

Component	Dimensions (depth,trans-axial,axial)	Parts (depth,trans-axial,axial)
Crystal	25 x 3.95 x 5.3	-
Submodule	25 x 16 x 15.9	1 x 4 x 3 Crystals
Module	25 x 64.5 x 47.8	1 x 4 x 3 Submodules
R Sector	25 x 64 .5 x 250.2	1 x 1 x 5 Modules
Ring	-	28 R Sectors

5.2.2   Digitizer

After doing the geometry, the digitizer module is the next step in order to define the simulation. The specifications include the energy resolution, the energy thresholds, the coincidence time window and the depth (readout level from which the coincidences are sorted). These values are all included on Table 5.2.

Table 5.2: Digitizer specifications of the GE Signa PET-MR Scanner

Energy resolution at 511 KeV	12% at FWHM
Energy threshold	425 – 650 KeV
Coincidence Time Window	4.57 ns
Depth	3

5.2.3   Other input parameters

Other parameters include the random generator. The engine chosen was MersenneTwister (default used in PET simulations) and the engine seed was set to auto which means that each time that GATE runs, it generates a new seed.

The outputs were the coincidence data ASCII file and a statistical file with the information of running times. No other output was chosen because it increases the simulation time and for this study the only data needed was the one with coincidences information, since it contains the coordinates values that are essential to obtain the sinograms.

5.3   Reconstruction

After simulating the data, the next step is to obtain the sinograms in order to perform the reconstruction and obtain images. The steps done to obtain the sinograms were all performed using MATLAB software and the reconstruction was done with STIR.

5.3.1   Coordinates algorithm

The output ASCII file contains the coincidence data. This file contains the arrival times, deposited energy and detection point coordinates and other quantities. All the values exist for both photons in each coincidence. From this file, the only information required was the photons coordinates.

In order to obtain a sinogram, an already existing MATLAB script, developed by Liliana Caldeira, had to be adapted to the output of GATE since it was prepared to be used with real data. Each crystal needs to be characterised by two coordinates (in the transaxial and axial directions) so that the script can be used

and the sinograms obtained. However, the GATE output (coincidences ASCII FILE) gives 4 coordinates:

- 1st coordinate = the position of the R Sector in the ring (R)

- 2nd coordinate = the position of the module in the R Sector (M)

- 3rd coordinate = the position of the submodule in the module (SM)

- 4th coordinate = the position of the crystal in the submodule (C)

The coordinates of each crystal within the module are given by Equation 5.1 (X coordinate) and Equation 5.2 (Y coordinate) calculated with the coordinates values given by the GATE output.

$$X = (i \times 4) + p \quad \text{where} \quad i = SM \bmod 4 \quad \text{and} \quad p = C \bmod 4 \tag{5.1}$$

$$Y = (j \times 4) + q \quad \text{where} \quad j = \frac{SM}{4} \quad \text{and} \quad q = \frac{C}{4} \tag{5.2}$$

Later, the coordinates of each crystal in the scanner are calculated with Equation 5.3 and 5.4. The X and Y values come from the equations mentioned before and the rest of the values come from the GATE output.

$$X_{Total} = (R \times 16) + X \tag{5.3}$$

$$Y_{Total} = (M \times 9) + Y \tag{5.4}$$

5.3.2 Sinograms

When a coincidence occurs, it is characterised by the line of response that connects the two detectors where each photon was detected. This line of response is characterised by the shortest distance between this line and the center of the scanner and by the angle of orientation of this line. Therefore, each coincidence is characterised by two values (distance and angle) that are organised in a matrix, forming sinograms that can be later used to do the reconstruction. After doing the coordinate transformation explained in the last section, these value were obtained.

As it was previously mentioned, a script, made by Liliana Caldeira, was provided in order to serve as base to obtain the sinograms. This script contained the equations used to calculate the angle of the line of response and its distance to the center. After calculating these parameters for every line of response and making some changes so the script could run, sinograms were obtained. However, before proceeding to the reconstruction, arc correction had to be made due to the the fact that the scanner has a ring shape.

5.3.3 Arc Correction

As it was mentioned previously (Section 2.3.2), due to the curved nature of the detector ring, the lines of response passing near the centre will be more distant from each other than the ones on the edge of the field of view. This needs to be corrected and it is called arc correction. The general objective is to rebine all the data in bins with the same width and this is applied before the reconstruction.

This correction was performed on MATLAB and all the steps are going to be explained in the next paragraphs. Firstly, the transverse geometry of the scanner needs to be represented on this software. One ring is enough in order to proceed with the correction. At the end of this stage, every crystal can be identified by two coordinates x and y. It is important to notice that all the gaps were simulated: the ones that exist between the submodules and those that exist between the modules (Figure 6.2 on the Appendix). Afterwards, all the lines of response that exist on that plane need to be found. The distance (Equations 5.5 to 5.8) and the angle to the center of the scanner (Equation 5.9) for each one of them are calculated in order to organise all the lines of response in a sinogram format.

Given two crystals A and B and their coordinates x and y, Equations 5.5 to 5.7 show how to calculate the coordinates of the middle point of the line segment that connects the two crystals.

$$\lambda = \frac{(x_{crystalA} - x_{crystalB}) * x_{crystalA} + (y_{crystalA} - y_{crystalB}) * y_{crystalA}}{(x_{crystalB} - x_{crystalA})^2 + (y_{crystalB} - y_{crystalA})^2} \tag{5.5}$$

$$x_p = x_{crystalA} + \lambda * (x_{crystalB} - x_{crystalA}) \tag{5.6}$$

$$y_p = y_{crystalA} + \lambda * (x_{crystalB} - x_{crystalA}) \tag{5.7}$$

From those coordinates it is possible to calculate the shortest distance between the line segment, that connects crystals A and B, and the center of the scanner with the expression showed on Equation 5.8.

$$dist(A, B) = \sqrt{x_p^2 + y_p^2}; \tag{5.8}$$

In order to calculate the angle, the expression that calculates the angle between a line segment and the x-axis is used. Given two crystals A and B and their coordinates x and y, equation 5.9 shows the angle that the line segment formed by those two crystals does with the scanner center.

$$theta(A, B) = \arctan\left(\frac{y_{crystalB} - y_{crystalA}}{x_{crystalB} - x_{crystalA}}\right) \tag{5.9}$$

Afterwards, a 2D sinogram is created from the distance and angle values calculated before. It is constituted by equally spaced bins that have an intensity showing how many lines of response pass through them. This is also known as 2D dwell map. In this step, it is defined the size of the distance and angle bins as wel as the number of bins in both directions.

Finally, the data from the uncorrected sinogram needs to be transferred to the arc corrected one. For each line of response, the bin in the uncorrected sinogram is found and its intensity is transferred to the bin that corresponds to that line of response in the arc corrected sinogram. Also, for each line of response a dwell correction was also done at the end in order to correct the multi-mapping situation when several lines of response are rebinned to one sinogram bin using the dwell map obtained before. In the end, all the data is distributed in equally spaced bins and the correction is finished.

5.3.4   STIR

Software for Tomographic Image Reconstruction (STIR) was the tool used to reconstruct the images. This software needs some inputs in order to proceed with the reconstruction: the normalisation sinogram (the only correction done), the prompts sinogram and a parameter file (.par) with input and output paths. There is also a bash file with the OSMAPOSL command and the path for the parameters file. In the next sections, the processes to obtain the inputs are explained.

5.3.4.1   Normalisation

One of the data corrections that had to be done was the normalisation correction. In order to do it, a simulation was performed using a cylinder with almost the size of the field of view. In this study, the cylinder source had 23 cm in the transaxial direction and 25 cm in the axial direction (covering the field of view). It was a back-to-back type of source with an activity of 0.1 MBq to reduce background noise.

The total simulation time was set to 720000 s. Since this was a long simulation, the cluster useded to perform the simulations before was not enough to perform this task. Therefore JURECA was used instead. JURECA is a supercomputer located in Forschungszentrum Juelich which greatest advantage is the capacity to analyse large volumes of data in a reasonable time frame.

Even though JURECA is a very powerful computer, the macro had to be split in 240 macros (72000 s each) distributed in 10 different jobs. Since each job has one node and the the maximum number of tasks per node is 24, the jobs were distributed this way in order to have the most efficiency.

After finishing the simulation, the obtained data went through the coordinates calculation, sinogram calculation and arc correction explained on Section 5.3.2. The normalisation arc corrected sinogram is displayed on Figure 5.2.
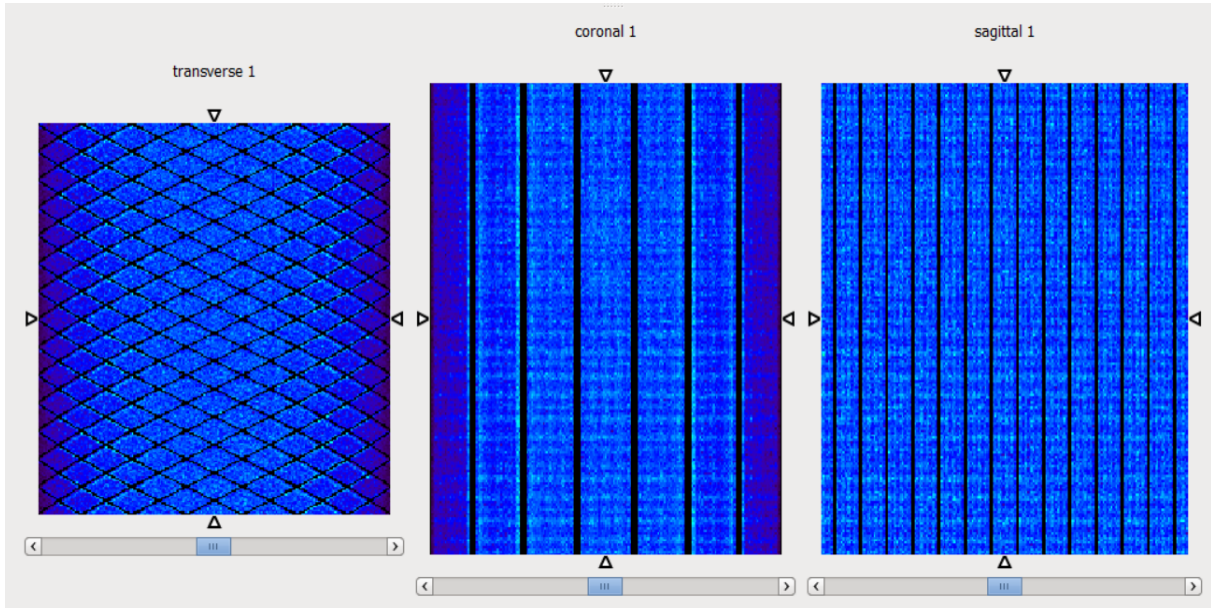
Figure 5.2: Normalisation sinogram in three different views (transverse, coronal and sagittal) visualised with the AMIDE software

Afterwards, a image of a cylinder with the dimensions of the cylinder used in the normalisation simulation was forward projected. Later, it is divided by the normalisation sinogram so the counts are distributed across all the sinogram. Before, there were a lot more counts in the middle than in the periphery of the sinogram even though the cylinder had uniform activity.

Considering that the GE Sigma PET-MR scanner has gaps, it can be challenging to do image reconstruction. The approach used in this thesis is called gap-masking and it was used in this study [53]. In this approach, after obtaining the final normalisation sinogram, a mask of the gaps was added to this sinogram. The gap detects zero events so it can be said that the sensitivity is 0 and the normalisation factor of the gap is infinite. So, the gaps were set to a very high number that should be infinity but since it is not possible, their values were set to 10^{29}.

The final normalisation sinogram can be seen on Figure 5.3. The red colour represents the gaps that have very high values, around 10^{29} (as it was set by the gap mask) and the black colour represents the coincidences registered that a very small value in comparison with the gaps. All the steps of the process that were done in order to obtain the final normalisation sinogram are summarised on Figure 5.4.

5.3.4.2   Header Files

All the sinograms inputs needed in order to perform the reconstruction on STIR require an header file. This file contains numerous parameters including the image modality, the corrections already applied to the data (arc correction), the image dimensions and the scanner parameters. Three of the four image dimensions come from the parameters that were defined in MATLAB in order to obtain the sinograms:
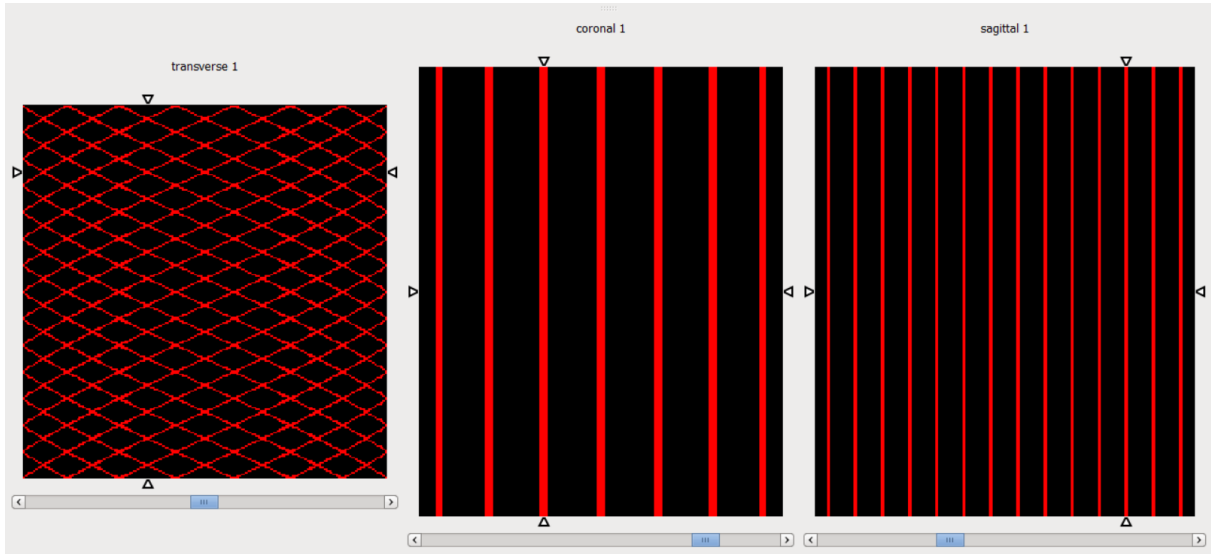
Figure 5.3: Normalisation sinogram used to do the normalisation correction in the image reconstruction. These images were obtained using the AMIDE software
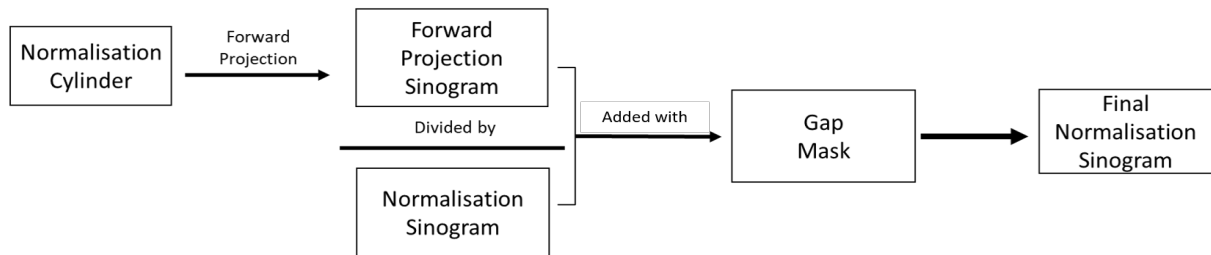

Figure 5.4: All the steps of the process that is done in order to obtain the final normalisation sinogram

the number of planes, distance and angle bins. The fourth dimension was also determined before and corresponds to the axial values.

There are two very important parameters that need to be determined, the minimum and maximum ring difference per segment. In order to obtain these values, a Michelogram needs to be computed. As previously said in Section 2.3.3, this is a 2D diagram in which each grid point corresponds to one ring pair and each oblique sinogram is represented by a line segment connecting two detector pairs. This can only be done if the span value is known and this value is equal to half of the difference between consecutive axials (it can also be known by calculating the ring difference between two adjacent segments if that parameter is known instead of the axials values). Span can be described as the number of sinograms that are mashed together and that have approximately the same axial angle, constituting a segment. The GE Signa PET-MR is a 45 ring scanner that uses a span of 2, has a maximum ring difference of 44 (minimum = -44) and 45 segments.

The scanner parameters include the number of rings and their dimensions, the distance between rings, the default bin size and the number of arc corrected bins. It also includes some geometry parameters that were defined in Section 5.2.1 like the number of crystals inside a submodule in both directions and the

number of submodules per module in both directions.

An header file for a offcenter cylinder sinogram is showed on Figure 6.1 on the Appendix. The headers of every sinogram must be correct in order to avoid errors, such as artefacts, before and after the reconstruction.

5.4   Offcenter Cylinder

A cylindrical source was simulated. This cylinder had a uniform geometry and activity making it easier to reconstruct. The simulated phantom had 11 cm of radius and an height of 25 cm. The cylinder height corresponds to the axial dimension of the scanner field of view. It was placed offcenter using the translation vector [5 5 0] cm. It was not placed in the center because this way we can see if the reconstruction is well oriented and if there are any artifacts related to the position of the source in the scanner.

The simulation parameters used were the ones mentioned in Section 5.2. The simulation time was set to 36000 s so we could get enough statistics for the reconstruction. The simulation was performed in JURECA since it has more computational power and therefore performed the simulation more quickly than in a local system.

5.4.1   Results and Discussion

After the simulation, the data stored in the coincidences ASCII file was sorted out so that the photons coordinates could be taken to a separate text file that can be read by MATLAB. Afterwards, the coordinates were ran through the coordinates algorithm (Section 5.3.3) in order to obtain the uncorrected sinogram (Figure 5.5). Subsequently, this data was used as input for the script that does the arc correction and a corrected sinogram, to be used in the reconstruction, was obtained and it is displayed on Figure 5.5, on the right.

From Figure 5.5 it can be seen the difference between the two sinograms in the transverse view: after doing the arc correction, the effect of the scanner gaps can be seen in the sinogram since the empty bins give a diamond shape to the cylinder data. Also, the sine wave shape has an higher amplitude in the corrected sinogram.

Afterwards, the reconstruction was performed on STIR. The inputs were the cylinder prompts arc corrected sinogram and the normalisation arc corrected sinogram (so that the normalisation correction could be performed) and that was showed previously on Figure 5.3. The resulting reconstruction (in different views) can be seen on Figure 5.6.
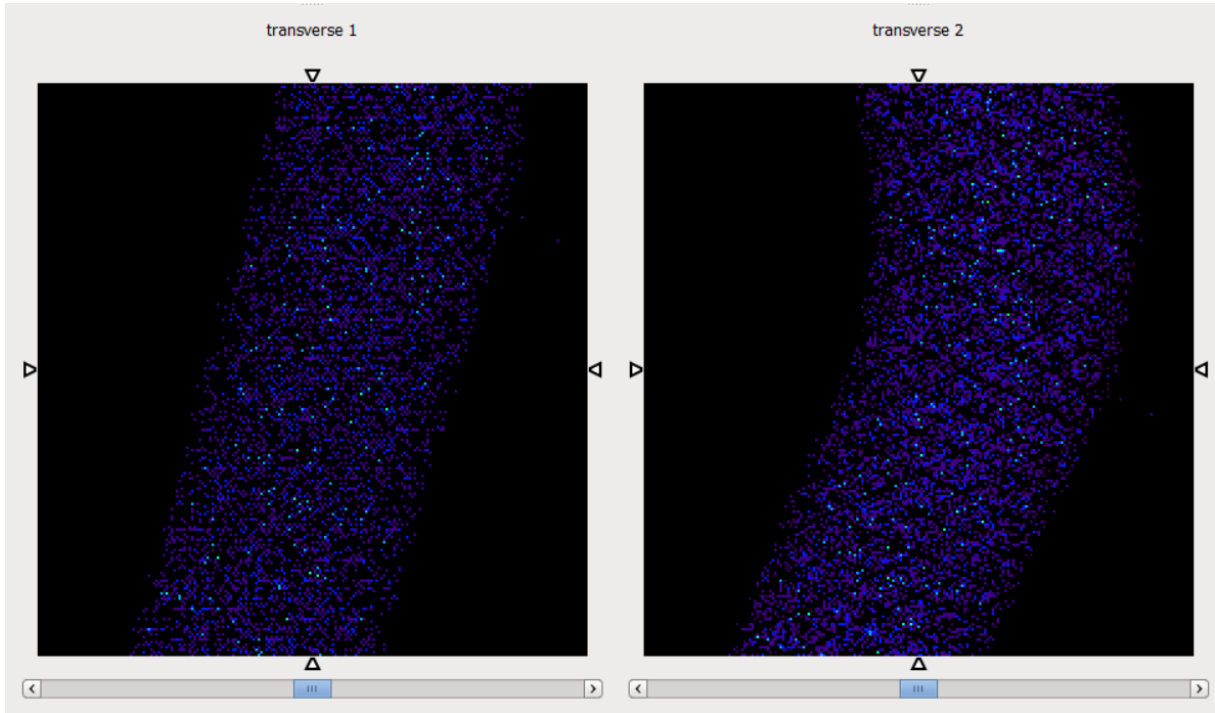
Figure 5.5: Transverse view of the offcenter cylinder uncorrected sinogram (on the left) and the arc corrected sinogram (on the right). Both images were obtained with AMIDE
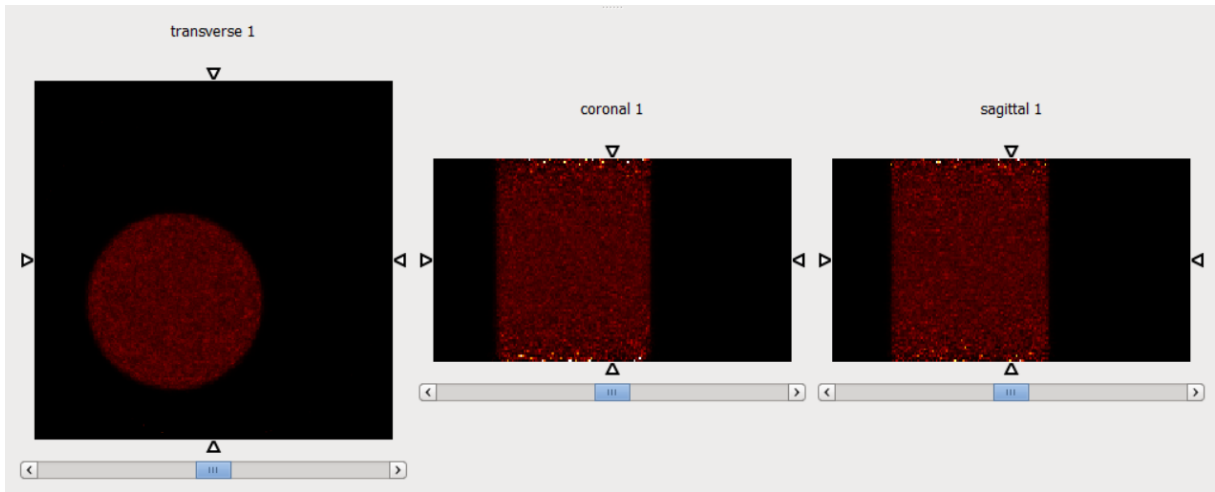

Figure 5.6: Reconstruction of an offcenter cylinder with a radius equal to 11 cm and placed according to the vector [5 5 0]cm, observed in three different views (transverse, coronal and sagittal) with AMIDE software

From Figure 5.6 one can see the reconstruction obtained from from the prompts of the simulated cylinder, without any visual artifact. However, it is positioned in the bottom half of the scanner, on the left when it should be represented on the upper half of the scanner on the right (because the translation vector was [5 5 0] cm). This is due to the fact that the scanner coordinates are not matching the sinogram coordinates so there is flip in the X and Y coordinates even though the reconstruction is still correct.

Afterwards, in order to see the effects of the corrections applied before the reconstruction, two reconstructions were performed. One of them was done without normalisation and the result is on Figure 5.7.
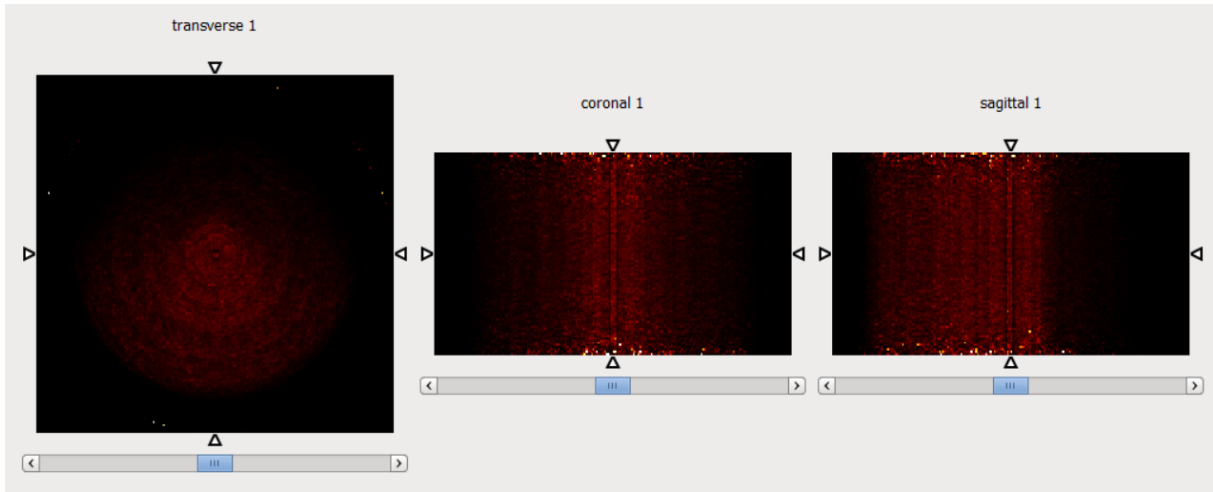
Figure 5.7: Reconstruction (without normalisation correction) of an offcenter cylinder with a radius equal to 11 cm and placed according to the vector [5 5 0]cm, observed in three different views (transverse, coronal and sagittal) with AMIDE software

From Figure 5.7 it can be seen what happens to reconstruction if normalisation correction is not applied. There are different "layers" of data in the cylinder and additionally, the cylinder was just partially reconstructed and in the center (instead of being offcenter).

The other reconstruction was performed with the uncorrected sinograms obtained before applying the arc correction. These sinograms do not take into account the existing scanner gaps and since they are obtained before arc correction, do not also take into account the fact that the bins are not equidistant. The result can be seen on Figure 5.8.
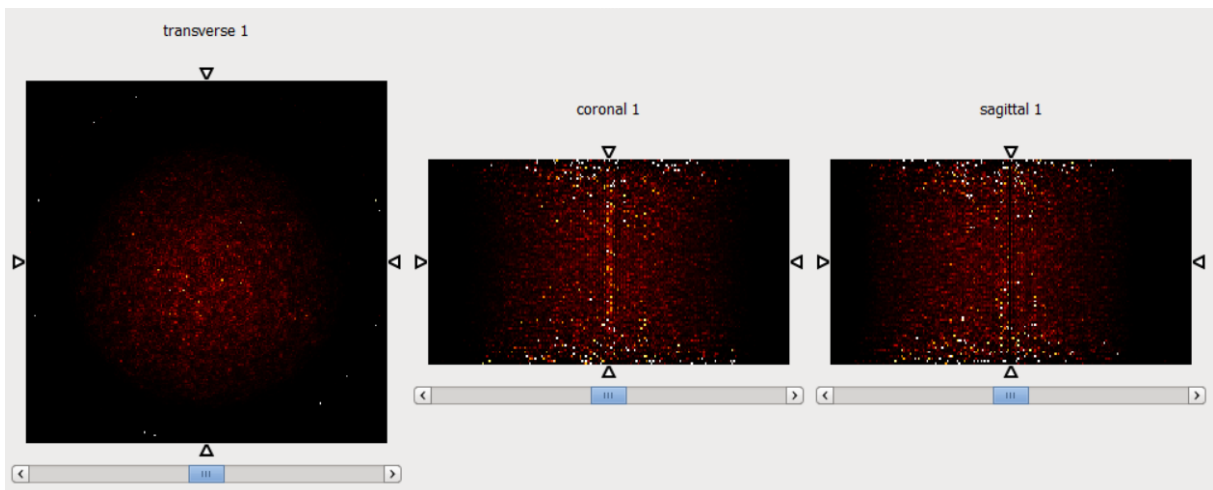

Figure 5.8: Reconstruction (without gaps and arc correction) of an offcenter cylinder with a radius equal to 11 cm and placed according to the vector [5 5 0]cm, observed in three different views (transverse, coronal and sagittal) with AMIDE software

From Figure 5.8 it can be seen the reconstruction of the offcenter cylinder using the uncorrected sino-

grams. The reconstruction does not show a well defined cylinder and additionally it is reconstructed in the center of the scanner. The data looks dispersed and without boundaries so it does not form a cylinder shape.

These last two reconstructions show the importance of doing corrections to the data before proceeding with the reconstruction. If not, the results will contain artifacts and will not correspond to the reality.

5.5   Hoffman Brain Phantom

After obtaining optimistic results with the cylinder source, it was time to try a more complex phantom. A Hoffman Brain Phantom was then simulated using JURECA so we could get faster results. The simulation parameters used were the ones mentioned in Section 5.2 and the simulation time was set to 36000 s in order to obtain enough data. The Hoffman Brain Phantom is constituted by an interfile image associated with a 3D raw image, a range translator and an activity translator table as it was already explained in detail on Section 4.1.2 (where it is also represented).

5.5.1   Results and Discussion

The procedure done here was the same that was done with the offcenter cylinder: the ASCII file was organised so that the photons coordinates could be ran through the coordinates algorithm; afterwards, the uncorrected sinogram was obtained (Figure 5.9 on the left) and the arc correction was applied so the corrected sinogram could be obtained (Figure 5.9 on the right). In Figure 5.9 it can be seen the difference
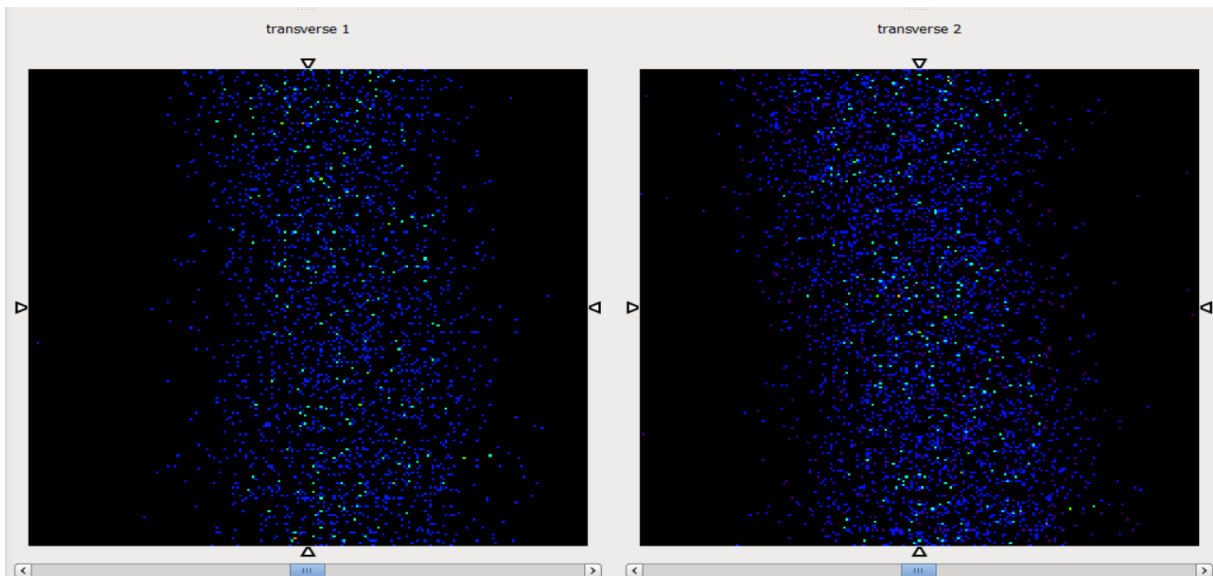

Figure 5.9: Transverse view of the Hoffman Brain Phantom uncorrected sinogram (on the left) and the arc corrected sinogram (on the right). Both images were obtained with AMIDE

between the uncorrected and arc corrected sinograms. The data is not as dispersed in the arc corrected sinogram as it is in the uncorrected one.

Afterwards, the reconstruction was performed on STIR. The inputs were the arc corrected sinogram of the phantom and the normalisation arc corrected sinogram (so that the normalisation correction could be performed). The resulting reconstruction (in different views) can be seen on Figure 5.10.
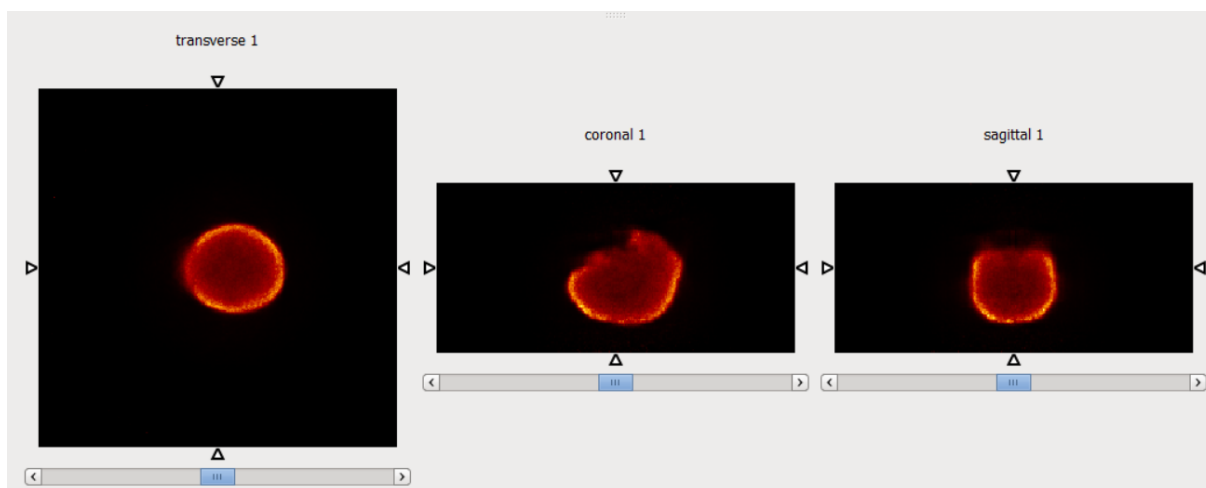

Figure 5.10: Reconstruction of an Hoffman Brain Phantom, observed in three different views (transverse, coronal and sagittal) with AMIDE software

From Figure 5.10 it can be seen the Hoffmann Brain Phantom reconstruction, without obvious visual artifacts from normalisation like it was previously obtained with the offcenter cylinder. The resulting images are low resolution as expected since no correction besides normalisation was done before reconstructing.

As it was done with the offcenter cylinder, two more reconstruction (without corrections) were done in order see the effects of the corrections applied before the reconstruction. On Figure 5.11 it can be seen the result of the reconstruction done without normalisation.

From Figure 5.11 it can be seen what happens to reconstruction if normalisation correction is not applied. In the transversal view, artifacts appear as circles on the left side of the phantom that propagate to the rest of the phantom. In the other views, the artifacts observed are vertical and horizontal lines with no data.

The other reconstruction was performed with the uncorrected sinograms obtained before applying the arc correction. As it was previously mentioned, these sinograms do not take into account the existing scanner gaps and since they are obtained before arc correction, do not also take into account the fact that the bins are not equidistant. The result can be seen on Figure 5.12.

From Figure 5.12 it can be seen the reconstruction of the offcenter cylinder using the uncorrected sino-
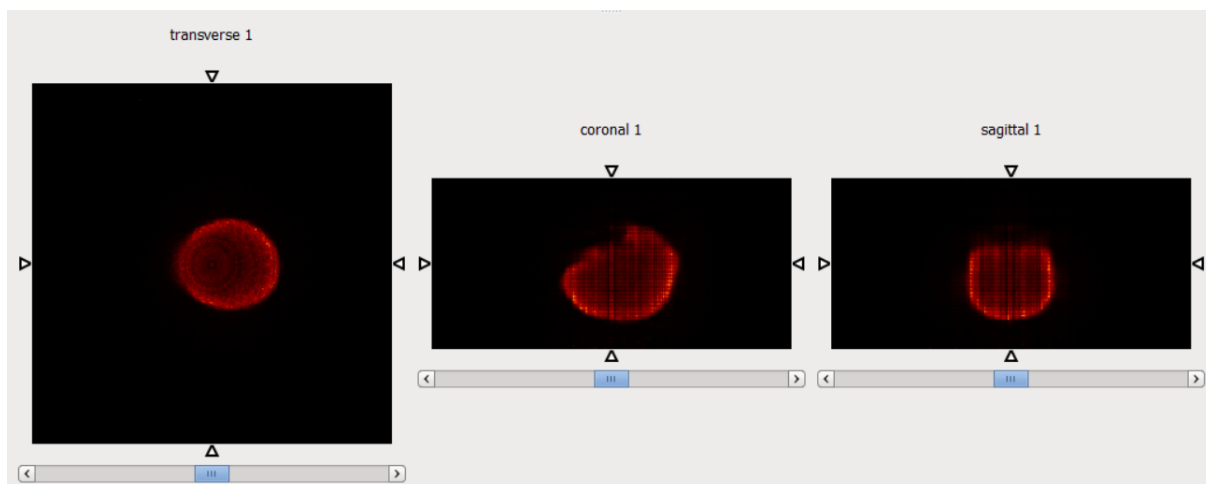
Figure 5.11: Reconstruction (without normalisation correction) of an Hoffman Brain Phantom, observed in three different views (transverse, coronal and sagittal) with AMIDE software
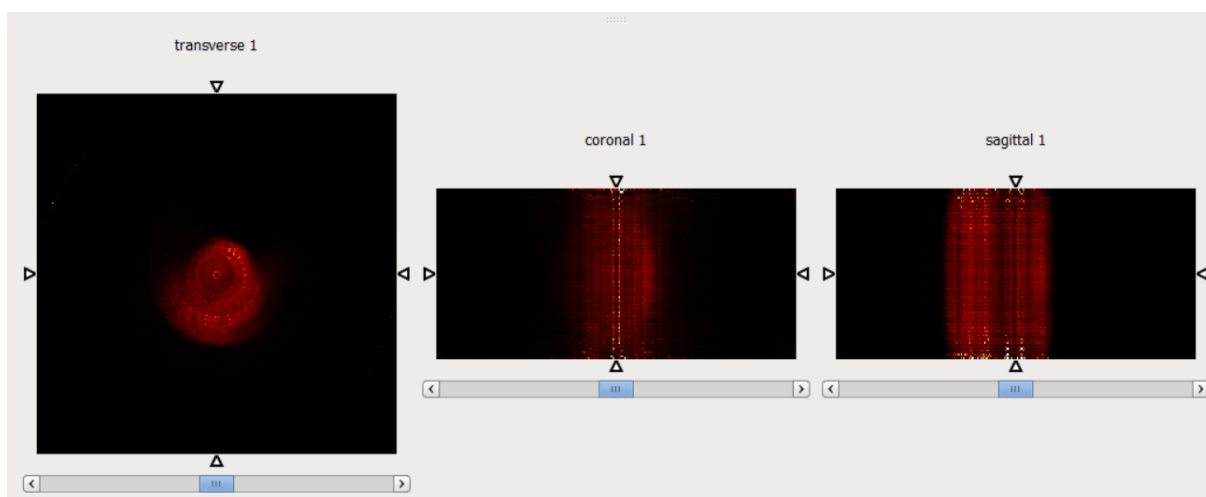

Figure 5.12: Reconstruction (without gaps and arc correction) of an Hoffman Brain Phantom, observed in three different views (transverse, coronal and sagittal) with AMIDE software

grams. The reconstruction does not look like the phantom being just an artifact in the middle of the image, on the tranverse view. On the other views, some artifact lines can also be seen. It is important to notice that the attenuation correction was not performed and as a result of that, the phantom looks bright on the edges and is not very homogeneous.

From these results it can be seen the importance of the corrections performed. In both phantoms, the usual reconstruction produced the expected results, obtaining good images of the phantom, validating the reconstruction proceedures. In the reconstructions without corrections, the results were also as expected: both phantoms appeared with a lot of artifacts that ruin the reconstruction.

Chapter 6

Conclusions

Time of flight is an important technique that has a lot of advantages when comparing to traditional PET. These advantages include having a more narrow coincidence window for whole-body imaging, reducing the number of random coincidences and improving the noise-equivalent-count, using LSO background transmission imaging as an input for simultaneous attenuation and activity reconstruction and improvement in signal-to-noise ratio when imaging large patients (due to the better localisation of coincidence events along the line of response). However, the method of trial and error can become very expensive when we are talking about scanner hardware and it is also time consuming. Simulation software, like for example GATE that offers a complete simulation from decay to detection, exist in order to test the changes to see if they work before making a decision to change in reality. Even within the software, there are easier and more time efficient methods to perform the simulations.

This thesis is made of two independent parts. The first part of this thesis focused on the possibility of using faster simulating methods. In this case, the possibility of replacing the time consuming GATE simulations by a script (that takes seconds to run) was studied. More specifically, is the possibility of getting the data of simulations with time resolution by just doing a GATE simulation without time resolution and running the script afterwards. After making the necessary changes so that the two methods have the same simulation parameters, the results show that the values obtained in the simulations with the Hoffman Brain Phantom are very similar between the two methods showing the viability of this script with this phantom. Then, the same procedure was performed using another Voxelized Brain Phantom. This time the results were not so good. In fact, the values obtained with the two methods show large differences. These results differ from those obtained with the previous phantom and question the viability of the script. However, the differences, for example in the number of randoms, come from the GATE

simulations and not from the script. The values from the script always show the expected behaviour. Therefore, it is important to know if there is some kind of problem with the phantom used that origins those results or if the problem comes from the script. It is important to notice that the script has very little guidelines and that are a few more parameters that were not studied beside the ones studied in this thesis (minimum sector difference and multiple policy).

The second part of this thesis focused on the development of reconstruction procedures for simulations done with GE Signa PET-MR scanner properties. After going through all the data treatment and corrections, two phantoms were reconstructed. The results show that the reconstructions were successful, without any artifacts. However, the resulting images of the Hoffman Brain Phantom had low resolution due to the fact that the only corrections made were arc correction and normalisation. The reconstructions done without each one of the corrections, show artifacts in both phantoms. These results show the importance of doing corrections before reconstructing the data. Future work includes trying the reconstruction with other types of phantoms, perform other types of corrections and do time of flight reconstruction since the scanner has time of flight capability.

References

[1] D. J. Brooks, "Positron emission tomography and single-photon emission computed tomography in central nervous system drug development," *NeuroRx*, vol. 2, no. 2, pp. 226–236, 2005.

[2] S. Jan, G. Santin, D. Strul, S. Staelens, K. Assie, D. Autret, S. Avner, R. Barbier, M. Bardies, P. Bloomfield, *et al.*, "Gate: a simulation toolkit for pet and spect," *Physics in Medicine & Biology*, vol. 49, no. 19, p. 4543, 2004.

[3] C. Weirich, D. Brenner, J. Scheins, É. Besancon, L. Tellmann, H. Herzog, and N. J. Shah, "Analysis and correction of count rate reduction during simultaneous mr-pet measurements with the brainpet scanner," *IEEE transactions on medical imaging*, vol. 31, no. 7, pp. 1372–1380, 2012.

[4] "Siemens biograph pet ct scanner." `https://www.indiamart.com/proddetail/siemens-biograph-pet-ct-scanner-17703064748.html`.

[5] "Siemens biograph mmr mr/pet scanner gets eu green light," Jun 2011. `https://www.medgadget.com/2011/06/siemens-biograph-mmr-mrpet-scanner-gets-eu-green-light.html`.

[6] E. Miele, G. P. Spinelli, F. Tomao, A. Zullo, F. De Marinis, G. Pasciuti, L. Rossi, F. Zoratto, and S. Tomao, "Positron emission tomography (pet) radiotracers in oncology–utility of 18f-fluoro-deoxy-glucose (fdg)-pet in the management of patients with non-small-cell lung cancer (nsclc)," *Journal of Experimental & Clinical Cancer Research*, vol. 27, no. 1, p. 52, 2008.

[7] G. Rees, A. Howseman, O. Josephs, C. D. Frith, K. J. Friston, R. S. Frackowiak, and R. Turner, "Characterizing the relationship between bold contrast and regional cerebral blood flow measurements by varying the stimulus presentation rate," *Neuroimage*, vol. 6, no. 4, pp. 270–278, 1997.

[8] "Fludeoxyglucose (18f)," Aug 2018. `https://en.wikipedia.org/wiki/Fludeoxyglucose_(18F)`.

[9] G. B. Saha, *Basics of PET imaging: physics, chemistry, and regulations*. Springer, 2015.

[10] S. R. Cherry, J. Sorenson, M. E. Phelps, and B. M. Methé, *Physics in nuclear medicine*, vol. 31. Wiley Online Library, 2004.

[11] G. F. Knoll, *Radiation detection and measurement*. John Wiley & Sons, 2010.

[12] Y. K. Kumar, S. B. Mehta, and U. Patil, "A review of epilepsy diagnosis using pet parameters," *Journal of Behavioral and Brain Science*, vol. 2, no. 03, p. 415, 2012.

[13] V. Vandenbussche, "Study and development of a pet device dedicated to cancer monitoring," 2014.

[14] P. Shreve and D. W. Townsend, *Clinical PET-CT in radiology: integrated imaging in oncology*. Springer Science & Business Media, 2010.

[15] S. Vandenberghe, E. Mikhaylova, E. D'Hoe, P. Mollet, and J. S. Karp, "Recent developments in time-of-flight pet.," *EJNMMI physics*, vol. 3 1, p. 3, 2016.

[16] E. Berg and S. R. Cherry, "Using convolutional neural networks to estimate time-of-flight from pet detector waveforms," *Physics in Medicine & Biology*, vol. 63, no. 2, p. 02LT01, 2018.

[17] M. Dahlbom, *Physics of PET and SPECT Imaging*. CRC Press, 2017.

[18] C. L. Melcher, "Scintillation crystals for pet," *Journal of Nuclear Medicine*, vol. 41, no. 6, pp. 1051–1055, 2000.

[19] B. Mazoyer, R. Trebossen, C. Schoukroun, B. Verrey, A. Syrota, J. Vacher, P. Lemasson, O. Monnet, A. Bouvier, and J. Lecomte, "Physical characteristics of ttv03, a new high spatial resolution time-of-flight positron tomograph," *IEEE Transactions on Nuclear Science*, vol. 37, no. 2, pp. 778–782, 1990.

[20] W. W. Moses and S. Derenzo, "Prospects for time-of-flight pet using lso scintillator," *IEEE Transactions on Nuclear Science*, vol. 46, no. 3, pp. 474–478, 1999.

[21] M. Daube-Witherspoon, S. Surti, A. Perkins, C. Kyba, R. Wiener, M. Werner, R. Kulp, and J. Karp, "The imaging performance of a labr3-based pet scanner," *Physics in Medicine & Biology*, vol. 55, no. 1, p. 45, 2009.

[22] S. Surti, J. Karp, G. Muehllehner, and P. Raby, "Investigation of lanthanum scintillators for 3d pet," in *Nuclear Science Symposium Conference Record, 2002 IEEE*, vol. 2, pp. 1177–1181, IEEE, 2002.

[23] S. Surti, A. Kuhn, M. E. Werner, A. E. Perkins, J. Kolthammer, and J. S. Karp, "Performance of philips gemini tf pet/ct scanner with special consideration for its time-of-flight imaging capabilities," *Journal of Nuclear Medicine*, vol. 48, no. 3, p. 471, 2007.

[24] V. C. Spanoudaki and C. S. Levin, "Photo-detectors for time of flight positron emission tomography (tof-pet)," *Sensors*, vol. 10, no. 11, pp. 10484–10505, 2010.

[25] T. Szczesniak, M. Moszynski, L. Swiderski, A. Nassalski, P. Lavoute, and M. Kapusta, "Fast photomultipliers for tof pet," *IEEE Transactions on Nuclear Science*, vol. 56, no. 1, pp. 173–181, 2009.

[26] A. Brahme, *Comprehensive biomedical physics*. Newnes, 2014.

[27] "Image galleries." `http://hamamatsu.magnet.fsu.edu/articles/avalanche.html`.

[28] "Introduction to pet physics: 2d mode and 3d mode." `https://depts.washington.edu/nucmed/IRL/pet_intro/intro_src/section3.html`.

[29] F. H. Fahey, "Data acquisition in pet imaging," *Journal of nuclear medicine technology*, vol. 30, no. 2, pp. 39–49, 2002.

[30] R. Buchert, K. H. Bohuslavizki, H. Fricke, J. Mester, and M. Clausen, "Performance evaluation of pet scanners: testing of geometric arc correction by off-centre uniformity measurement," *European journal of nuclear medicine*, vol. 27, no. 1, pp. 83–90, 2000.

[31] J. Tian, *Molecular imaging: Fundamentals and applications*. Springer Science & Business Media, 2013.

[32] D. L. Bailey, M. N. Maisey, D. W. Townsend, and P. E. Valk, *Positron emission tomography*. Springer, 2005.

[33] M. Defrise, P. E. Kinahan, and C. J. Michel, *Image reconstruction algorithms in PET*. Springer, 2005.

[34] R. Badawi and P. Marsden, "Developments in component-based normalization for 3d pet," *Physics in Medicine & Biology*, vol. 44, no. 2, p. 571, 1999.

[35] Y. Chen and H. An, "Attenuation correction of pet/mr imaging," *Magnetic Resonance Imaging Clinics*, vol. 25, no. 2, pp. 245–255, 2017.

[36] S. Moehrs, M. Defrise, N. Belcari, A. Del Guerra, A. Bartoli, S. Fabbri, and G. Zanetti, "Multi-ray-based system matrix generation for 3d pet reconstruction," *Physics in Medicine & Biology*, vol. 53, no. 23, p. 6925, 2008.

[37] S. Tong, A. M. Alessio, and P. E. Kinahan, "Image reconstruction for pet/ct scanners: past achievements and future challenges," *Imaging in medicine*, vol. 2, no. 5, p. 529, 2010.

[38] Palisade, "What is monte carlo simulation?." `http://www.palisade.com/risk/monte_carlo_simulation.asp`.

[39] "Pseudorandom number generator," Aug 2018. `https://en.wikipedia.org/wiki/Pseudorandom_number_generator`.

[40] "Pseudo random number generator (prng)," Jun 2017. `https://www.geeksforgeeks.org/pseudo-random-number-generator-prng/`.

[41] M. Haahr, "True random number service." `https://www.random.org/randomness/`.

[42] K. Chan, S. M. Heng, and R. Smee, "Application of monte carlo simulation in treatment planning for radiation oncology," in *Applications of Monte Carlo Methods in Biology, Medicine and Other Fields of Science*, InTech, 2011.

[43] I. Buvat and D. Lazaro, "Monte carlo simulations in emission tomography and gate: An overview," *Nuclear Instruments and Methods in Physics Research Section A: Accelerators, Spectrometers, Detectors and Associated Equipment*, vol. 569, no. 2, pp. 323–329, 2006.

[44] H. Herzog, K.-J. Langen, J. Kaffanke, C. Weirich, I. Neuner, G. Stoffels, E. R. Kops, J. Scheins, L. Tellmann, and N. J. Shah, "Mr-pet opens new horizons in neuroimaging," *Future Neurology*, vol. 5, no. 6, pp. 807–815, 2010.

[45] H. Herzog, K.-J. Langen, C. Weirich, E. R. Kops, J. Kaffanke, L. Tellmann, J. Scheins, I. Neuner, G. Stoffels, K. Fischer, *et al.*, "High resolution brainpet combined with simultaneous mri," *Nuklearmedizin*, vol. 50, no. 02, pp. 74–82, 2011.

[46] H. Herzog, L. Tellmann, B. Marx, E. R. Kops, J. Scheins, C. Weirich, and N. Shah, "Performance tests and preliminary results of the 3tmr-brainpet scanner installed at the forschungszentrum jülich," in *World Congress on Medical Physics and Biomedical Engineering, September 7-12, 2009, Munich, Germany*, pp. 677–680, Springer, 2009.

[47] C. Catana, T. Benner, A. van der Kouwe, L. G. Byars, M. S. Hamm, D. B. Chonde, C. J. Michel, G. N. E. Fakhri, M. Schmand, and A. G. Sorensen, "Mri-assisted pet motion correction for neurologic studies in an integrated mr-pet scanner.," *Journal of nuclear medicine : official publication, Society of Nuclear Medicine*, vol. 52 1, pp. 154–61, 2011.

[48] A. Kolb, H. F. Wehrl, M. Hofmann, M. S. Judenhofer, L. Eriksson, R. Ladebeck, M. P. Lichy, L. Byars, C. Michel, H.-P. Schlemmer, *et al.*, "Technical performance evaluation of a human brain pet/mri system," *European radiology*, vol. 22, no. 8, pp. 1776–1788, 2012.

[49] I. Buvat, S. Jan, S. Kerhoas, F. Mayet, *et al.*, "Users guide v8.0: From gate collaborative documentation wiki," *no. July*, 2011.

[50] A. M. Grant, T. W. Deller, M. M. Khalighi, S. H. Maramraju, G. Delso, and C. S. Levin, "Nema nu 2-2012 performance studies for the sipm-based tof-pet component of the ge signa pet/mr system," *Medical physics*, vol. 43, no. 5, pp. 2334–2343, 2016.

[51] M. Khalifé, S. Stute, A. Wagadarikar, S. Jan, and C. Comtat, "Modeling the ge signa pet-mr with monte carlo simulations using gate," 2015.

[52] C. S. Levin, S. H. Maramraju, M. M. Khalighi, T. W. Deller, G. Delso, and F. Jansen, "Design features and mutual compatibility studies of the time-of-flight pet capable ge signa pet/mr system.," *IEEE Trans. Med. Imaging*, vol. 35, no. 8, pp. 1907–1914, 2016.

[53] L. Caldeira, C. Weirich, P. Almeida, and H. Herzog, "Reconstruction of pet data acquired with the brainpet using stir," in *Nuclear Science Symposium and Medical Imaging Conference (NSS/MIC), 2012 IEEE*, pp. 2327–2329, IEEE, 2012.

Appendix

```
!INTERFILE :=
!imaging modality:= PT
name of data file := norm_corrected_215_224_1981.fs
originating system := Userdefined
!version of keys := STIR3.0
!GENERAL DATA :=
!GENERAL IMAGE DATA :=
!type of data := PET
imagedata byte order := LITTLEENDIAN
!PET STUDY (General) :=
!PET data type := Emission
applied corrections := {arc correction}
!number format := float
!number of bytes per pixel := 4
number of dimensions := 4
matrix axis label [4] := segment
!matrix size [4] := 45
matrix axis label [2] := view
!matrix size [2] := 224
matrix axis label [3] := axial coordinate
!matrix size [3] :=
{ 89,85,85,81,81,77,77,73,73,69,69,65,65,61,61,57,57,53,53,49,49,
45,45,41,41,37,37,33,33,29,29,25,25,21,21,17,17,13,13,9,9,5,5,1,1
}
matrix axis label [1] := tangential coordinate
!matrix size [1] := 215
minimum ring difference per segment :=
{ -1,-3,2,-5,4,-7,6,-9,8,-11,10,-13,12,-15,14,-17,16,-19,18,-21,2
0,-23,22,-25,24,-27,26,-29,28,-31,30,-33,32,-35,34,-37,36,-39,38,
-41,40,-43,42,-44,44}
maximum ring difference per segment :=
{ 1,-2,3,-4,5,-6,7,-8,9,-10,11,-12,13,-14,15,-16,17,-18,19,-20,21
,-22,23,-24,25,-26,27,-28,29,-30,31,-32,33,-34,35,-36,37,-38,39,-
40,41,-42,43,-44,44}
Scanner parameters:=
Scanner type := Userdifined
Number of Rings                          := 45
Number of detectors per ring             := 448
Inner ring diameter (cm)                 := 62.36
Average depth of interaction (cm)        := 0
Distance between rings (cm)              := 0.556
Default bin size (cm)                    := 0.204
Maximum number of non-arc-corrected bins := 215
Default number of arc-corrected bins     := 215
Number of blocks per bucket in transaxial direction  := 4
Number of blocks per bucket in axial direction       := 3
Number of crystals per block in axial direction      := 3
Number of crystals per block in transaxial direction := 4
Number of detector layers                            := 1
end Scanner parameters:=
effective central bin size (cm)      := 0.204
number of time frames                := 1
!END OF INTERFILE :=
```
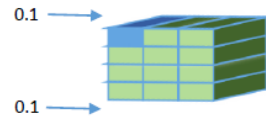
Figure 6.1: Header file of the prompts sinogram of the offcenter cylinder that was used in the reconstruction
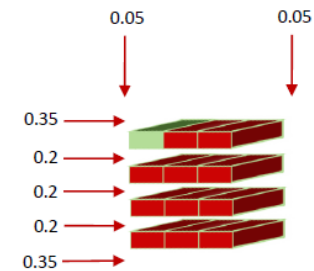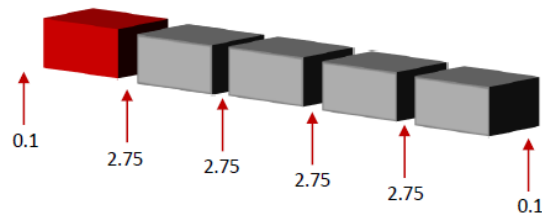
GE Signa Scanner

0.05   0.05

0.1

0.1

0.35
0.2
0.2
0.2
0.35
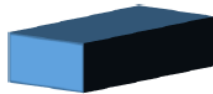
Crystal dimensions
25 x 3.95 x 5.3

Submodule dimensions
1 x 4 x 3 crystals = 25 x (15.8 + 0.1 x 2) x 15.9

Module dimensions
1 x 4 x 3 submodules = 25 x (64 + 0.25 x 2) x
(47.7 + 0.05 x 2)

0.1   2.75   2.75   2.75   2.75   0.1

R Sector dimensions
1 x 1 x 5 modules = 25 x 64.5 x (239 + 2.75 * 4 +
0.1*2)

Figure 6.2: 3D drawings and measurements of each component of the GE Signa PET-MR scanner